Shell model study of using an effective field theory for disentangling several contributions to neutrinoless double-β decay

Mihai Horoi and Andrei Neacsu

Phys. Rev. C **98**, 035502 — Published 4 September 2018

DOI: 10.1103/PhysRevC.98.035502

Shell model study of using an effective field theory for disentangling several contributions to the neutrinoless double-beta decay

Mihai Horoi* and Andrei Neacsu†
Department of Physics, Central Michigan University, Mount Pleasant, Michigan 48859, USA
(Dated: August 9, 2018)

Weak interaction in nuclei represents a well-known venue for testing many of the fundamental symmetries of the Standard Model. In particular, neutrinoless double-beta decay offers the possibility to test Beyond Standard Model theories predicting that neutrinos are Majorana fermions and the lepton number conservation is violated. This paper focuses on an effective field theory approach to neutrinoless double-beta decay for extracting information regarding the properties of the Beyond Standard Model Lagrangian responsible for this process. We use shell model nuclear matrix elements and the latest experimental lower limits for the half-lives to extract 12 lepton number violating parameters of five nuclei of experimental interest, and lower limits for the energy scales of the new physics. Using the most stringent limits that we obtain for the values of the lepton number violating parameters, we predict new half-life limits for the other nuclei of experimental interest, in the case of 12 neutrino double-beta decay mechanisms. We provide an analysis that could reveal valuable information regarding the dominant neutrinoless double-beta decay mechanism, if experimental half-life data becomes available for different isotopes.

I. INTRODUCTION

The experimental discovery of neutrino oscillations [1, 2] was awarded the Nobel prize in 2015 [3, 4] for clarifying some of the properties of neutrinos. The important consequence of these observations is that neutrinos have non-zero mass. However, oscillation experiments alone can only measure squared mass differences, while other neutrino properties such as their mass hierarchy, their absolute masses, or their nature (whether neutrinos are Dirac or Majorana fermions) remain elusive. Nevertheless, the success of these experiments has greatly increased the interest in neutrino physics in general, and neutrinoless double-beta decay ($0\nu\beta\beta$) in particular.

The neutrinoless double-beta decay ($0\nu\beta\beta$) is considered the best approach to study the yet unknown properties of neutrinos related to their nature, whether they are Dirac or Majorana fermions, which the neutrino oscillation experiments cannot clarify. Should the neutrinoless double-beta transitions occur, then the lepton number conservation is violated by two units, and the black-box theorems [5–8] indicate that the light left-handed neutrinos are Majorana fermions. As such, through black-box theorems alone, it is not possible to disentangle the dominant mechanism contributing to this process. Most of the theoretical effort dedicated to this subject consists of calculations of leptonic phase-space factors and nuclear matrix elements that are computed via several nuclear structure methods and within specific models. One of the most popular models is the left-right symmetric model [9–13], which is currently investigated at the Large Hadron Collider (LHC) [14]. In two recent papers [15, 16] we have discussed ways to identify some of the possible contributions to the decay rate by studying the angular distribution and the energy distribution of the two outgoing electrons that could be measured. However, there are still many other possible contributions to this process that one cannot yet dismiss. For these reasons, a more general beyond standard model (BSM) effective field theory would be preferable, as it would not be limited to relying on specific models, but rather considering the most general BSM effective field theoretical approach that describes this process. An important outcome of such a theory is the evaluation of the energy scales up to which the effective field operators are not broken, together with limits for the effective low-energy couplings.

The analysis of the $0\nu\beta\beta$ decay process is generally done at three levels. At the lowest level the weak interaction of the quarks and leptons is considered and the BSM physics is treated within a low-energy effective field theory approach. At the next level the hadronization process to nucleons and exchanging pion is considered. The nucleons are treated in the impulse approximation leading to free space $0\nu\beta\beta$ transition operators. At the third level the nucleon dynamics inside the nuclei is treated using nonperturbative nuclear wave functions, which are further used to obtain nuclear matrix elements (NME) needed to calculate the $0\nu\beta\beta$ observables, such as half-lives and two-electron angular and energy distributions [15]. A modern approach that could accomplish this plan would be based on the chiral effective field theory of pions and nucleons [17, 18]. This approach introduces a number of couplings, which in principle can be calculated from the underlying theory of strong interaction using lattice QCD techniques [17], or may be extracted within some approximation from the known experimental data [18]. These couplings may come with new phases and they may include effective contributions from the exchange of heavier mesons. The lattice QCD approach is underway, but it proved to be very difficult for extracting even basic weak nucleon couplings, such as g_A [19].

* mihai.horoi@cmich.edu
† neacs1a@cmich.edu

In this paper we start from the formalism of Ref. [20–23] that provides a general effective field theory (EFT) approach to the neutrinoless double-beta decay. However, at the hadron level three new diagrams are added for the first time to the effective field theory analysis of the $0\nu\beta\beta$, which were only considered in the literature in the context of specific mechanisms. Under the assumption that a single coupling in the BSM Lagrangian dominates the $0\nu\beta\beta$ amplitude, we extract new limits for the effective Majorana mass and for 11 additional low-energy EFT couplings using data from five nuclei of current experimental interest. Some of these couplings correspond to parameters found in left-right symmetric models, and we present and compare them. To be able to get the limits of these effective couplings and parameters from the experimental half-life limits, 20 nuclear matrix elements (NME) and 9 phase-space factors (PSF) are needed. Finally, we use the limits for the EFT couplings and the formalism of the effective field theory to obtain limits for the energy scale of the new physics that could be responsible for the neutrinoless double beta decay process.

We further extend the use of the EFT to calculate and study the half-life ratios for pairs from a number of five experimentally interesting isotopes in the case of all 12 lepton number violating couplings. The ratio of half-lives can be used to probe the sensitivity of the five isotopes in relation to their respective mechanisms and to predict the half-life limits needed to match the different experimental results. This information could be useful in estimating scales and costs, fine-tuning the experiments in search for the $0\nu\beta\beta$ transition mechanism that is expected to produce the shortest half-life, but also to get a better view and compare the status of various experiments. Even more interesting is that in the case of experimental confirmation of $0\nu\beta\beta$ for different isotopes, one could possibly indicate the dominant mechanism of the transition.

To accomplish this goal we need reliable NME. The most commonly used nuclear structure methods for the NME calculation are proton-neutron Quasi Random Phase Approximation (pnQRPA) [20–28], Interacting Shell Model (ISM) [29–47], Interacting Boson Model (IBM-2) [48–51], Projected Hartree Fock Bogoliubov (PHFB) [52], Energy Density Functional (EDF) [53], and the Relativistic Energy Density Functional (REDF) [54] method. The NME calculated with different methods and by different groups sometimes show large differences, and this has been debated in the literature [55, 56]. Although there seem to exist many NME results to choose from, most of the references listed only provide calculations for the light left-handed Majorana neutrino exchange. Ref. [45] provides tables and plots that compare the latest results for the light left-handed neutrino exchange and for the heavy right-handed neutrino exchange.

The NME used in Ref. [20–23] come from older QRPA calculations, which do not include many of the improvements proposed in recent years [57, 58]. We calculate the NME using shell model techniques, which are consistent with previous calculations [31, 36–46]. The reason for choosing shell model NME is our belief that these are better suited and more reliable for $0\nu\beta\beta$ calculations, as they take into account all the correlations around the Fermi surface, respect all symmetries, and take into account consistently the effects of the missing single particle space via many-body perturbation theory (the effects were shown to be small, about 20%, for ^{82}Se [59]). Furthermore, we have tested the shell model methods and the effective Hamiltonians used by comparing calculations of spectroscopic observables to the experimental data, as presented in Ref. [36, 45, 60]. We do not consider any quenching for the bare $0\nu\beta\beta$ operator in these calculations. Such a choice is different from that for the simple Gamow-Teller operator used in the single beta and $2\nu\beta\beta$ decays where a quenching factor of about 0.7 is necessary [61]. For the PSF we use an effective theory based on the formalism of Ref. [62], but fine-tuned as to take into account the effects of a Coulomb field distorting finite-size proton distribution in the final nucleus. To our knowledge, two of the NME presented in this paper are calculated for the first time using shell model techniques.

When studying the half-life ratios, we found that the choice of effective Hamiltonians plays an important role in the analysis. If the NME of the two isotopes that enter the ratio can be calculated both within the same model space using the same effective Hamiltonian, the uncertainties in our analysis are insignificant. On the other hand, when the NME require different Hamiltonians and especially used in different model spaces, then extra care needs to be given to those calculations. For these reasons, in the analysis of the half-life ratios, we take into account two sets of effective Hamiltonians and their corresponding optimal closure energies [38, 40, 43], $\langle E\rangle$, specific for each model space. One set of NME is obtained using the Hamiltonians preferred by our group, and the results are designated by the "CMU" label. For ^{48}Ca in the pf model space $(0f_{7/2}, 1p_{3/2}, 0f_{5/2}, 1p_{1/2})$ we use GXPF1A [63] with $\langle E\rangle = 0.5$ MeV, for ^{76}Ge and ^{82}Se in the $jj44$ model space $(0f_{5/2}, 1p_{3/2}, 1p_{1/2}, 0g_{9/2})$ we choose JUN45 [64] with $\langle E\rangle = 3.4$ MeV, and for ^{130}Te and ^{136}Xe in the $jj55$ model space $(0g_{7/2}, 1d_{5/2}, 1d_{3/2}, 1s_{1/2}, 0h_{11/2})$ we use SVD [65] with $\langle E\rangle = 3.5$ MeV. The second set of NME we calculate using the Hamiltonians preferred by the Strasbourg-Madrid group, and denoted with "St-Ma". In this case, for ^{48}Ca we use KB3G [66] with $\langle E\rangle = 2.5$ MeV, for ^{76}Ge and ^{82}Se GCN.28-50 with $\langle E\rangle = 10$ MeV, and for ^{130}Te and ^{136}Xe we use GCN.50-82 with $\langle E\rangle = 12$ MeV.

This paper is organized as follows: Section II analyzes the contributions of several BSM mechanisms to the neutrinoless double-beta decay. Section III presents the framework of the effective field theory for the neutrinoless double-beta decay. Section IV shows the experimental limits on the BSM lepton number violating (LNV) couplings that we calculate, and is divided into three subsec-

tions. Subsection IV A is dedicated to revisit of the most common approach to $0\nu\beta\beta$ that considers only the light left-handed Majorana neutrino exchange, presenting shell model nuclear matrix elements and upper limits for the Majorana mass. Subsection IV B details the study of the long-range contributions to the $0\nu\beta\beta$ decay Lagrangian. Subsection IV C presents the analysis of the short-range contribution LNV parameters. Section V contains our analysis of half-life ratios. The calculated half-lives that are expected to match the sensitivity of KamLand-Zen are shown in Subsection V A and a possible way to find the dominant mechanism is presented in Subsection V B. Discussions are presented in Section VI, Section VII is dedicated to conclusions and, last, Section VIII is an Appendix containing all the relevant formulae for calculating the NME.

II. BSM MECHANISMS CONTRIBUTING TO NEUTRINOLESS DOUBLE-BETA DECAY

The main mechanism considered to be responsible for the neutrinoless double beta decay is the mass mechanism that assumes that the neutrinos are Majorana fermions, and relies on the assumption that the light left-handed neutrinos have mass. However, the possibility that right-handed currents could contribute to the neutrinoless double-beta decay ($0\nu\beta\beta$) has been already considered for some time [62, 73]. Recently, $0\nu\beta\beta$ studies [13, 74] have adopted the left-right symmetric model [11, 75] for the inclusion of right-handed currents. In addition, the R-parity violating ($\not{R}_p$) supersymmetric (SUSY) model can also contribute to the neutrinoless double beta decay process [76–78]. In the framework of the left-right symmetric model and R-parity violating SUSY model, the $0\nu\beta\beta$ half-life can be written as a sum of products of PSF, BSM LNV parameters, and their corresponding NME [15]:

$$\left[T^{0\nu}_{1/2}\right]^{-1} = G_{01} g_A^4 \left|\eta_{0\nu} M_{0\nu} + \left(\eta^L_{N_R} + \eta^R_{N_R}\right) M_{0N} + \eta_{\tilde{q}} M_{\tilde{q}} + \eta_{\lambda'} M_{\lambda'} + \eta_\lambda X_\lambda + \eta_\eta X_\eta\right|^2 . \quad (1)$$

Here, G_{01} is a phase-space factor that can be calculated with good precision for most cases [67, 79–81], g_A is the axial vector coupling constant, $\eta_{0\nu} = \frac{\langle m_{\beta\beta}\rangle}{m_e}$, with $\langle m_{\beta\beta}\rangle$ representing the effective Majorana neutrino mass, and m_e the electron mass. $\eta^L_{N_R}$, $\eta^R_{N_R}$ are the heavy neutrino parameters with left-handed and right-handed currents, respectively [13, 31], $\eta_{\tilde{q}}$, $\eta_{\lambda'}$ are $\not{R}_p$ SUSY LNV parameters [82], η_λ, and η_η are parameters for the so-called "$\lambda-$" and "$\eta-$mechanism", respectively [13]. $M_{0\nu}$, M_{0N}, are the light and the heavy neutrino exchange NME, $M_{\tilde{q}}$, $M_{\lambda'}$ are the $\not{R}_p$ SUSY NME, and X_λ and X_η denote combinations of NME and other PSF ($G_{02} - G_{09}$) corresponding to the $\lambda-$mechanism involving right-handed leptonic and right-handed hadronic currents, and the $\eta-$mechanism with right-handed leptonic and left-handed hadronic currents, respectively [15]. Assuming a seesaw type I dominance [83], the term $\eta^L_{N_R}$ is considered not to contribute if the heavy mass eigenstates are larger than 1 GeV [47], and we neglect it here. For consistency with the literature, the remaining term $\eta^R_{N_R}$ is labeled as η_{0N}. In Eq. (1) and in all equations describing half-lives below, we factorize $g_A^4 = 1.27^4$ just to be consistent with the most recent definitions of the PSF [67, 79–81]. Our view is that if there is any quenching, that is not of the g_A, but rather due to the methodology of calculating the NME.

In Table I we present the $Q^{0\nu}_{\beta\beta}$ values, the most recent experimental half-life limits from the indicated references, and the nine PSF for $0\nu\beta\beta$ transitions to ground states of the daughter nucleus for five isotopes currently under investigation. The PSF were calculated using a new effective method described in great detail in Ref. [81]. G_{01} values were calculated with a screening factor (s_f) of 94.5, while for $G_{02} - G_{09}$ we used $s_f = 92.0$ that was shown to provide results very close to those of Ref. [84]. We note that the ^{82}Se experimental half-life used here and throughout this analysis is preliminary [70]. However, we believe that this limit is valid and that it may get improved.

In Ref. [15] we show how one could disentangle contributions form different mechanisms using two-electron angular and energy distributions, as well as half-life data from several isotopes. Here, we consider the case where one mechanism dominates, more explicitly, one single term in the decay amplitude of Eq. (1). Table II shows the shell model values of the NME that enter Eq. (1). The light and heavy neutrino-exchange NME, $M_{0\nu}$ and M_{0N}, are taken from Ref. [44] that describes their formalism and calculation. $M_{\tilde{q}}$ and $M_{\lambda'}$ are calculated using the description in Eq. (150) and Eq. (155), respectively, of Ref. [82]. X_λ and X_η are adapted from C_4 and C_5 of Eq. (3.5.15d) and Eq. (3.5.15e), respectively, in Ref. [62] multiplied by M_{GT}/G_{01} to fit the factorization of Eq. (1). All NME used in this paper were calculated using the interacting shell model (ISM) approach [31, 38–41, 44, 47] (see Ref. [44] for a review), and include short-range-correlation effects based on the CD-Bonn parametrization [36], finite-size effects [82] and, when appropriate, optimal closure energies [60] (see Appendix for more details).

The upper limits for corresponding LNV parameters extracted from lower limits of the half-lives under the assumption that only one term in the amplitude dominates, are also presented in Table II. There are a few other QRPA [62, 82, 84–86] and ISM [29–32] results in the literature that were obtained within the framework of the LRSM and SUSY. However, some of the extracted LNV parameters rely on some older half-life limits.

One of the main advantages of using models is that one can relate the neutrino physics parameters, $\eta_{0\nu}$, $\eta^L_{N_R}$, $\eta^R_{N_R}$, etc, to the underlying model parameters, such as masses, mixing angles, etc [13, 15, 82]. However, the models mentioned above provide a limited (incomplete)

TABLE I. The $Q^{0\nu}_{\beta\beta}$ values in MeV, the experimental $T^{0\nu}_{1/2}$ limits in years, and the calculated PSF ($G_{01} - G_{09}$) in years^{-1} for all five isotopes currently under investigation.

	^{48}Ca	^{76}Ge	^{82}Se	^{130}Te	^{136}Xe
$Q^{0\nu}_{\beta\beta}$ [67]	4.272	2.039	2.995	2.527	2.458
$T^{0\nu}_{1/2}$ >	2.0×10^{22} [68]	8.0×10^{25} [69]	2.5×10^{23} [70]	4.0×10^{24} [71]	1.07×10^{26} [72]
$G_{01} \times 10^{14}$	2.45	0.23	1.00	1.41	1.45
$G_{02} \times 10^{14}$	15.5	0.35	3.21	3.25	3.15
$G_{03} \times 10^{15}$	18.2	1.20	6.50	8.46	8.55
$G_{04} \times 10^{15}$	5.04	0.42	1.92	2.53	2.58
$G_{05} \times 10^{13}$	3.28	0.60	2.16	4.12	4.36
$G_{06} \times 10^{12}$	3.87	0.50	1.66	2.16	2.21
$G_{07} \times 10^{10}$	2.85	0.28	1.20	1.76	1.80
$G_{08} \times 10^{11}$	1.31	0.17	0.82	1.72	1.83
$G_{09} \times 10^{10}$	15.6	1.12	4.42	4.47	4.44

TABLE II. The NME that appear in Eq. (1) for the five nuclei of current experimental interest, and the corresponding LNV parameters extracted under the assumption that only one dominates.

	^{48}Ca	^{76}Ge	^{82}Se	^{130}Te	^{136}Xe
$M_{0\nu}$	1.02	3.63	3.40	1.92	1.74
M_{0N}	81.4	196	181	126	113
$M_{\tilde{q}}$	107	339	320	185	169
$M_{\lambda'}$	162	418	395	245	222
X_λ	2.11	4.12	5.68	2.81	2.48
X_η	243	784	716	510	462
$10^6 \times \lvert\eta_{0\nu}\rvert$	27.3	0.40	3.65	1.36	0.28
$10^9 \times \lvert\eta_{0N}\rvert$	343.8	7.42	68.5	20.6	4.40
$10^9 \times \lvert\eta_{\tilde{q}}\rvert$	260	4.28	38.8	14.1	2.95
$10^9 \times \lvert\eta_{\lambda'}\rvert$	172.8	3.47	31.4	10.7	2.24
$10^7 \times \lvert\eta_\lambda\rvert$	133	3.52	21.88	9.30	2.01
$10^9 \times \lvert\eta_\eta\rvert$	115	1.85	17.3	5.12	1.08

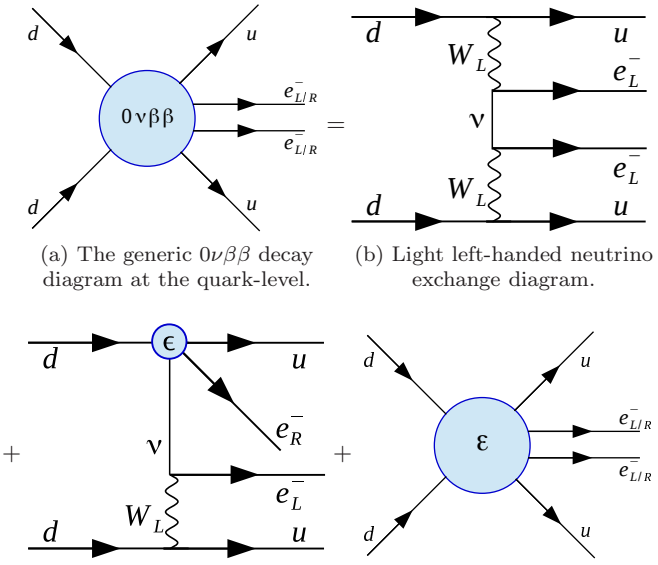

(a) The generic $0\nu\beta\beta$ decay diagram at the quark-level.

(b) Light left-handed neutrino exchange diagram.

(c) The long-range part of the $0\nu\beta\beta$ diagram.

(d) The short-range part of the $0\nu\beta\beta$ diagram.

FIG. 1. The $0\nu\beta\beta$ decay process diagrams: (1a) presents the generic description of the process, (1b) shows the most studied case in the literature, that of the light left-handed neutrino exchange, (1c) is the long-range component of the $0\nu\beta\beta$ decay diagram, while (1d) displays the short-range part.

number of Lorentz invariant terms in the low energy Lagrangian that induces contributions to the neutrinoless double beta decay amplitudes.

III. EFFECTIVE FIELD THEORY APPROACH TO NEUTRINOLESS DOUBLE-BETA DECAY

A more general approach is based on the effective field theory extension of the Standard Model. The analysis based on the BSM contributions to the effective field theory is more desirable, because it does not rely on specific models, and their parameters could be extracted/constrained by the existing $0\nu\beta\beta$ data, and by data from LHC and other experiments. In fact, the models considered in section II always lead to a subset of terms in the low-energy ($\sim$ 200 MeV) effective field theory Lagrangian. Here we consider all the terms in the Lagrangian allowed by the symmetries. Some of the couplings will correspond to the model couplings in Eq. (1), but they might have a wider meaning. Others are new, not corresponding to specific models.

At the quark-level, we present in Figure 1 the generic $0\nu\beta\beta$ Feynman diagrams contributing to the $0\nu\beta\beta$ process. We consider contributions coming from the light left-handed Majorana neutrino (Fig. 1b), a long-range part coming from the low-energy four-fermion charged-current interaction (Fig. 1c), and a short-range part (Fig. 1d).

We treat the long-range component of the $0\nu\beta\beta$ diagram as two point-like vertices at the Fermi scale, which

exchange a light neutrino. In this case, the dimension 6 Lagrangian can be expressed in terms of effective couplings [23]:

$$\mathcal{L}_6 = \frac{G_F}{\sqrt{2}}\left[j^{\mu}_{V-A}J^{\dagger}_{V-A,\mu} + \sum_{\alpha,\beta}^{*}\epsilon^{\beta}_{\alpha}j_{\beta}J^{\dagger}_{\alpha}\right], \qquad (2)$$

where $J^{\dagger}_{\alpha} = \bar{u}\mathcal{O}_{\alpha}d$ and $j_{\beta} = \bar{e}\mathcal{O}_{\beta}\nu$ are hadronic and leptonic Lorentz currents, respectively. The definitions of the $\mathcal{O}_{\alpha,\beta}$ operators are given in Eq. (3) of Ref. [23]. The LNV parameters are $\epsilon^{\beta}_{\alpha} = \{\epsilon^{V+A}_{V-A},\ \epsilon^{V+A}_{V+A},\ \epsilon^{S+P}_{S\pm P},\ \epsilon^{TR}_{TR}\}$. The "*" symbol indicates that the term with $\alpha = \beta = (V-A)$ is explicitly taken out of the sum. However, the first term in Eq. (2) still entails BSM physics through the dimension-5 operator responsible for the Majorana neutrino mass (see also section VI). Here $G_F = 1.1663787 \times 10^{-5}$ GeV^{-2} denotes the Fermi coupling constant. Refs. [20–23] also include a ϵ^{TL}_{TR} contribution. We recently found [87] that this contribution is actually zero, and we removed it from our analysis.

As already mentioned, some of these couplings play the same role as some of the model couplings listed in Eq. (1), but they have more general meaning here. For example, ϵ^{V+A}_{V-A} play the same role as η_{η} and ϵ^{V+A}_{V+A} play the same role as η_{λ} in the effective Lagrangian associated to models.

In the short-range part of the diagram presented in Fig. 1d we consider the interaction to be point-like. Expressing the general Lorentz-invariant Lagrangian in terms of effective couplings [22], we get:

$$\mathcal{L}_9 = \frac{G_F^2}{2m_p}\Big[\varepsilon_1 JJj + \varepsilon_2 J^{\mu\nu}J_{\mu\nu}j + \varepsilon_3 J^{\mu}J_{\mu}j + \varepsilon_4 J^{\mu}J_{\mu\nu}j^{\nu} + \varepsilon_5 J^{\mu}Jj_{\mu}\Big], \qquad (3)$$

with the hadronic currents of defined chirality $J = \bar{u}(1\pm\gamma_5)d$, $J^{\mu} = \bar{u}\gamma^{\mu}(1\pm\gamma_5)d$, $J^{\mu\nu} = \bar{u}\frac{i}{2}[\gamma^{\mu},\gamma^{\nu}](1\pm\gamma_5)d$, leptonic currents $j = \bar{e}(1\pm\gamma_5)e^C$, $j^{\mu} = \bar{e}\gamma^{\mu}(1\pm\gamma_5)e^C$, and $\varepsilon^{\beta}_{\alpha} = \varepsilon^{xyz}_{\alpha} = \{\varepsilon_1,\ \varepsilon_2,\ \varepsilon_3^{LLz(RRz)},\ \varepsilon_3^{LRz(RLz)},\ \varepsilon_4,\ \varepsilon_6\}$. These parameters have dependence on the chirality of the hadronic and the leptonic currents involved, with $xyz = L/R, L/R, L/R$. In the case of ε_3, one can distinguish between different chiralities, thus we express them separately as $\varepsilon_3^{LLz(RRz)}$ and $\varepsilon_3^{LRz(RLz)}$.

The contribution of the diagrams 1b and 1c to the $0\nu\beta\beta$ decay amplitude is proportional to the time-ordered product of two effective $\mathcal{L}_6$ Lagrangians [23],

$$T(\mathcal{L}_6^{(1)}\mathcal{L}_6^{(2)}) = \frac{G_F^2}{2}T\Big[j_{V-A}J^{\dagger}_{V-A}j_{V-A}J^{\dagger}_{V-A} + \epsilon^{\beta}_{\alpha}j_{\beta}J^{\dagger}_{\alpha}j_{V-A}J^{\dagger}_{V-A} + \epsilon^{\beta}_{\alpha}\epsilon^{\delta}_{\gamma}j_{\beta}J^{\dagger}_{\alpha}j_{\delta}J^{\dagger}_{\gamma}\Big], \qquad (4)$$

while the contribution of the diagram 1d is proportional to $\mathcal{L}_9$. This description of the effective Lagrangian contributing to the decay misses the specificity of the ϵ/ε parameters to any underlying physics/model, but they can be used to assess the scale of the BSM physics (see section VI).

However, when calculating the $0\nu\beta\beta$ half-life it is necessary to identify the contributions corresponding to different hadronization prescriptions. Figure 2 shows the nucleon-level diagrams in a similar way to Figure 1. The first 3 contributions, Figs. 2b, 2c, and 2d are similar to the corresponding amplitudes at the quark level (see Fig. 1). In addition to these contributions that were also considered in Ref. [23], here we also include the long range diagrams that involve pion(s) exchange, Figs. 2e, 2f, and 2g. These diagrams were considered before as contributing to the $0\nu\beta\beta$ decay rate, but in the context of $\not{R}_p$ SUSY mechanism. For example, the diagram 2e was considered to describe the contribution of the squark-exchange mechanism [78], and the diagrams 2f and 2g were considered to describe the contribution of the gluino exchange mechanism [88]. One should also mention that the diagram 2g was also considered in Refs. [89, 90], but its contribution to the $0\nu\beta\beta$ half-life was estimated differently, and cannot be directly compared to the other contributions analyzed here.

After hadronization (see Fig. 2), the extra terms in the Lagrangian require the knowledge of 20 individual NME [21–23, 76, 82, 91]. We can write the half-life in a factorized compact form

$$\left[T^{0\nu}_{1/2}\right]^{-1} = g_A^4\left[\sum_i |\mathcal{E}_i|^2\,\mathcal{M}_i^2 + \mathrm{Re}\left[\sum_{i\neq j}\mathcal{E}_i\mathcal{E}_j\mathcal{M}_{ij}\right]\right]. \qquad (5)$$

Here, the $\mathcal{E}_i$ contain the neutrino physics parameters, with $\mathcal{E}_1 = \eta_{0\nu}$ representing the exchange of light left-handed neutrinos corresponding to Fig. 2b, $\mathcal{E}_{2-6} = \{\epsilon^{V+A}_{V-A},\ \epsilon^{V+A}_{V+A},\ \epsilon^{S+P}_{S\pm P},\ \epsilon^{TR}_{TR},\ \eta_{\pi\nu}\}$ are the long-range LNV parameters appearing in Figs. 2c and 2e, and $\mathcal{E}_{7-14} = \{\varepsilon_1,\ \varepsilon_2,\ \varepsilon_3^{LLz(RRz)},\ \varepsilon_3^{LRz(RLz)},\ \varepsilon_4,\ \varepsilon_5,\ \eta_{1\pi},\ \eta_{2\pi}\}$ denote the short-range LNV parameters at the quark level involved in the diagrams of Fig. 2d, 2f, 2g. The rational for including the $\eta_{\pi\nu}$ in the same class with the LNV entering the quark-level long range diagrams is that Ref. [78] indicates that $\eta_{\pi\nu}$ is proportional to ϵ^{TR}_{TR} (see Section IV B below). In the same vein, Ref. [88] indicates that ε_1 and ε_2 are proportional to a combination of $\eta_{1\pi}$ and $\eta_{2\pi}$ (see Section IV C below). Therefore the $\eta_{1\pi}$ and $\eta_{2\pi}$ were included in the list LNV couplings associated with quark-level short-range diagrams. Contributions of pion-exchange diagrams similar to those of Figs. 2f and 2g are also included in the so called "higher order term in nucleon currents" [82]. However, they are constrained by PCAC, and are only included in light-neutrino exchange contribution of diagram 2a. This contribution changes the associated NME by only 20%. Therefore, we conclude that this does not represent a serious double counting issue.

Following Refs. [21–23, 82], we write $\mathcal{M}_i^2$ as combinations of NME described in Eqs. (8, 10, 12, 14, and 16) (see also Eq.(20) in the Appendix for the individual NME) and integrated PSF [81] denoted with $G_{01} - G_{09}$.

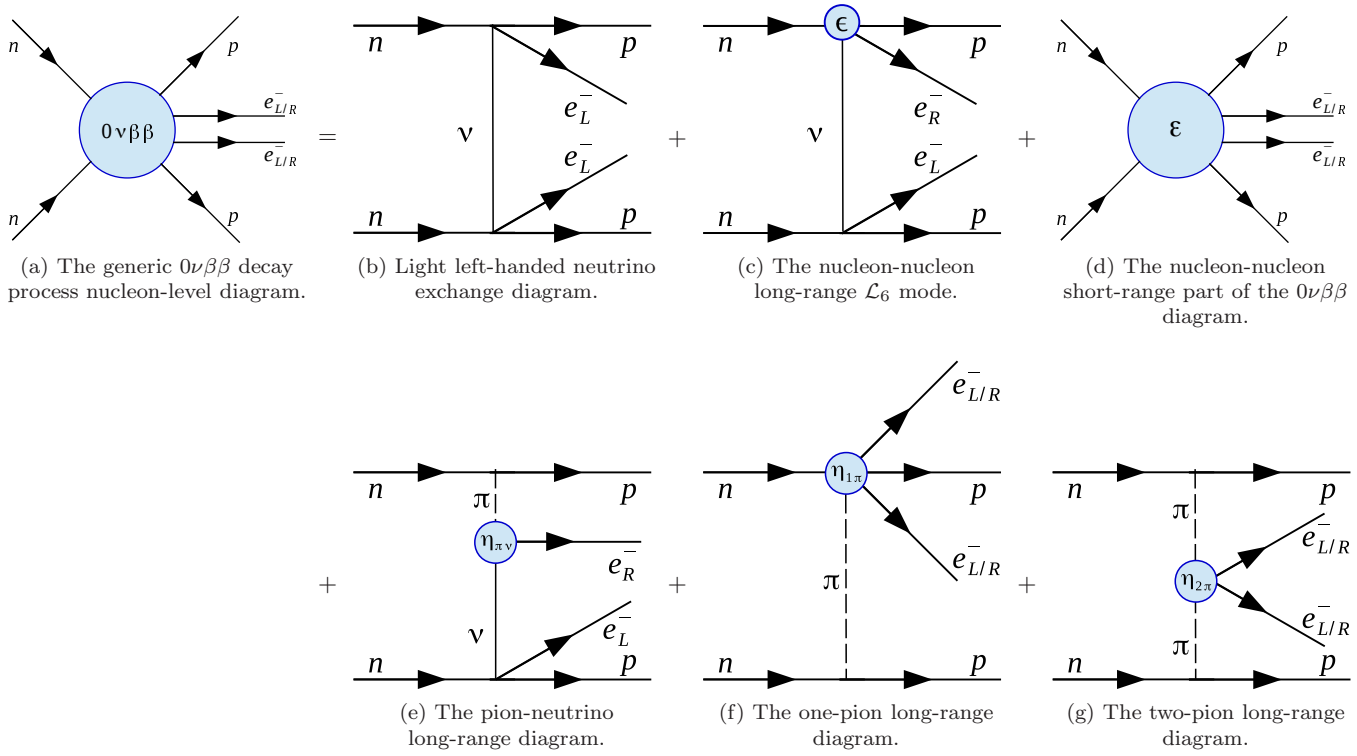

(a) The generic $0\nu\beta\beta$ decay process nucleon-level diagram.

(b) Light left-handed neutrino exchange diagram.

(c) The nucleon-nucleon long-range $\mathcal{L}_6$ mode.

(d) The nucleon-nucleon short-range part of the $0\nu\beta\beta$ diagram.

(e) The pion-neutrino long-range diagram.

(f) The one-pion long-range diagram.

(g) The two-pion long-range diagram.

FIG. 2. Similar to Fig.1, we present the nucleon-level diagrams of $0\nu\beta\beta$ decay process : (2a) presents the generic description of the process, (2b) shows the light left-handed neutrino exchange, (2c) is the long-range component, Subfigure 2d shows the short-range contribution. On the second line, (2e) is the pion-neutrino component, (2f) is the one-pion long-range contribution of the $\mathcal{R}_p$ SUSY induced $0\nu\beta\beta$ diagram, and (2g presents the two-pion long-range contribution of the $\mathcal{R}_p$ SUSY induced $0\nu\beta\beta$. The effective couplings $\eta_{1\pi}$ and $\eta_{2\pi}$ are related to Eq. (16) as $\eta_{1\pi} = c_{1\pi}\eta_{\pi N}$ and $\eta_{2\pi} = c_{2\pi}\eta_{\pi N}$.

Our values of the PSF are presented in Table I. In some cases the interference terms $\mathcal{E}_i\mathcal{E}_j\mathcal{M}_{ij}$ are small [92] and can be neglected, but not all of them. In Ref. [15] we analyzed a subset of terms contributing to the half-life formula, Eq. (1) originating from the left-right symmetric model. In that restrictive case we showed that one can disentangle different contributions to the $0\nu\beta\beta$ decay process using two-electron angular and energy distributions as well as half-lives of two selected isotopes. Obviously, this number of observables is not enough to extract all coupling appearing in the effective field theory Lagrangian. However, they can be used to constrain these couplings, thus adding to the information extracted from the Large Hadron Collider and other related experiments. Here we attempt to extract these couplings assuming that only one of them can have a dominant contribution to the half-life, Eq. (5). We call this approach "on-axis". Considering the "on-axis" approach to extracting limits of the LNV parameters, the interference terms are neglected in our analysis. In the following, we extract the "on-axis" upper limits of these parameters using the most recent experimental half-lives lower limits, as presented in Table I.

IV. EXPERIMENTAL LIMITS ON THE BSM LNV COUPLINGS

To obtain experimentally constrained upper limits of the effective LNV couplings one needs experimental half-life lower limits, accurate calculations of the PSF, together with reliable NME results calculated using nuclear structure methods tested to correctly describe the experimental nuclear structure data available for the nuclei involved. We split our analysis of the LNV parameters into three subsections corresponding the exchange of light left-handed Majorana neutrinos, the LNV couplings entering the remaining quark-level long-range diagrams, and the LNV couplings entering the quark-level short-range diagrams.

A. The exchange of light left-handed neutrinos

Most studies in the literature have considered just the case where only the exchange of light left-handed Majorana neutrinos contribute to the $0\nu\beta\beta$ decay process, presented in Figs. 1b and 2b. Therefore, one can easily find calculations of NME and PSF for this scenario.

TABLE III. The first line shows values of the $\mathcal{M}^2_{0\nu}$ coefficients containing combinations of NME and PSF, and the second line presents the extracted neutrino physics parameter $|\eta_{0\nu}|$ for the most studied case, assuming only the exchange of light left-handed Majorana neutrinos.

	^{48}Ca	^{76}Ge	^{82}Se	^{130}Te	^{136}Xe
$\mathcal{M}^2_{0\nu}\times10^{14}$	2.57	3.00	11.5	5.22	4.40
$\lvert\eta_{0\nu}\rvert\times10^{6}$	27.3	0.40	3.65	1.36	0.28

Considering this case, we reduce the half-life equation to:

$$\left[T^{0\nu}_{1/2}\right]^{-1} = g_A^4 \left|\eta_{0\nu}\right|^2 \mathcal{M}^2_{0\nu}, \tag{6}$$

where $g_A = 1.27$, $\mathcal{M}^2_{0\nu}$ contains the coefficients containing combinations of NME and PSF (see Eq. (8) below). $\eta_{0\nu} = \frac{\langle m_{\beta\beta}\rangle}{m_e}$, where m_e is the electron mass and $\langle m_{\beta\beta}\rangle$ represents the effective Majorana neutrino mass described as [74]:

$$\langle m_{\beta\beta}\rangle = \left|\sum_{j=1}^{3} U^2_{ej} m_j\right|. \tag{7}$$

Here U_{ej} are the PMNS mixing matrix elements [93, 94] and the summation is performed over all the three light neutrino mass eigenstates m_j. Also in Eq. (6)

$$\mathcal{M}^2_{0\nu} = G_{01}\left[M_{GT} - \left(\frac{g_V}{g_A}\right)^2 M_F + M_T\right]^2, \tag{8}$$

where $g_V = 1$ is the vector coupling constant, $g_A = 1.27$ is the axial coupling constant, and G_{01} is the phase-space factor. The three NME, M_{GT}, M_F, and M_T (shown in Table XV) correspond to the Gamow-Teller, Fermi and Tensor transition operators, respectively, and are described in the Appendix. All the NME listed in the tables of the Appendix have the correct signs relative to that of M_{GT}, which is chosen to be positive. The $\mathcal{M}^2$ coefficients correctly include these relative signs, but the overall sign of the $\mathcal{M}$ in Eqs. (8, 10, 12, 14, and 16) is lost due to squaring.

In Table III we present the $\mathcal{M}^2_{0\nu}$ values and their corresponding $\eta_{0\nu}$ limits. We find the lowest upper-limit of this parameter for ^{136}Xe, which leads to a limit for the Majorana neutrino mass $\langle m_{\beta\beta}\rangle \sim 140$ meV.

B. The long-range effective LNV couplings

Investigating the "on-axis" LNV parameters of the diagram of Fig. 2c, the half-life is factorized as:

$$\left[T^{0\nu}_{1/2}\right]^{-1} = g_A^4 \left[\left|\epsilon^{\beta}_{\alpha}\right|^2 \mathcal{M}^2_{\alpha\beta}\right], \tag{9}$$

with $\epsilon^{\beta}_{\alpha} = \{\epsilon^{V+A}_{V-A},\ \epsilon^{V+A}_{V+A},\ \epsilon^{S+P}_{S\pm P},\ \epsilon^{TR}_{TR}\}$. Here and below the $\alpha\beta$ combination corresponds to some index i in Eq. (5), as described in the definition of $\mathcal{E}_i$ after Eq. (5). Following the formalism presented in Refs. [21, 23, 62] and including the $G_{01} - G_{09}$ PSF, we write the long-range coefficients containing combinations of NME and PSF as:

$$\begin{aligned}
\mathcal{M}^2_{V+A/V-A} &= G_{02}\mathcal{M}^2_{2+} - \frac{2}{9}G_{03}\mathcal{M}_{1-}\mathcal{M}_{2+} + \frac{1}{9}G_{04}\mathcal{M}^2_{1-} \\
&\quad - G_{07}M_P M_R + G_{08}M^2_P + G_{09}M^2_R, \qquad (10a)\\
\mathcal{M}^2_{V+A/V+A} &= G_{02}\mathcal{M}^2_{2-} \\
&\quad - \frac{2}{9}G_{03}\mathcal{M}_{1+}\mathcal{M}_{2-} + \frac{1}{9}G_{04}\mathcal{M}^2_{1+}, \qquad (10b)\\
\text{with } \mathcal{M}_{1\pm} &= M_{GTq} \pm 3\left(\frac{g_V}{g_A}\right)^2 M_{Fq} - 6M_{Tq} \\
\text{and } \mathcal{M}_{2\pm} &= M_{GT\omega} \pm \left(\frac{g_V}{g_A}\right)^2 M_{F\omega} - \frac{1}{9}\mathcal{M}_{1\pm}, \\
\mathcal{M}^2_{S+P/S\pm P} &= \left(\frac{F^{(3)}_P}{R m_e g_A}\right)^2 G_{01}\left(M_{T'} + \frac{1}{3}M_{GT'}\right)^2, \qquad (10c)\\
\mathcal{M}^2_{TR/TR} &= \left(\frac{4T^{(3)}_1 g_V(1+(\mu_p-\mu_n))}{R m_e g^2_A}\right)^2 \\
&\quad \times G_{01}\left(M_{T'} - \frac{2}{3}M_{GT'}\right)^2. \qquad (10d)
\end{aligned}$$

In these equations, $R = 1.2A^{1/3}$ fm is the nuclear radius, $m_e = 0.511$ MeV is the electron mass, $m_\pi = 139$ MeV is the pion mass, $m_p = 938$ MeV is the proton mass, $(\mu_p - \mu_n) \simeq 3.7$, and the parameters $F^{(3)}_P = 4.41$, $T^{(3)}_1 = 1.38$ are taken from Ref. [95] where they have been calculated using the MIT bag model. Detailed expressions for the individual M_α (with $\alpha = GTq$, Fq, Tq, $GT\omega$, $F\omega$, P, R, GT', T') are found in the Appendix.

It is possible to obtain another limit for ϵ^{TR}_{TR} by considering a different hadronization procedure [78] depicted in Fig. 2e, where our $\eta_{\pi\nu}$ plays the same role as $\eta^{11}_{(q)LR}$ in Eq.(22) of Ref. [78]. In this case we can obtain an alternative value for ϵ^{TR}_{TR}, $\tilde{\epsilon}^{TR}_{TR} = \eta_{\pi\nu}/8$.

$$\left[T^{0\nu}_{1/2}\right]^{-1} = g_A^4 \left[\left|8\ \tilde{\epsilon}^{TR}_{TR}\right|^2 \mathcal{M}^2_{\pi\nu}\right], \tag{11}$$

with

$$\mathcal{M}^2_{\pi\nu} = G_{01}\left[M_{GT\pi\nu} + M_{T\pi\nu}\right]^2. \tag{12}$$

The $M_{GT\pi\nu}$ and $M_{T\pi\nu}$ are the same NME as $M_{GT(\tilde{q})}$ and $M_{T(\tilde{q})}$ in Eq.(155) of Ref.[82] (also described in the Appendix).

Table IV shows our shell model $\mathcal{M}^2_{\alpha\beta}$ coefficients. We present our values for the long-range LNV parameters in Table V, where $\tilde{\epsilon}^{TR}_{TR}$ represents the alternative limit for ϵ^{TR}_{TR} that is obtained using $\mathcal{M}_{\pi\nu}$. With the exception of ^{48}Ca, the $\tilde{\epsilon}^{TR}_{TR}$ upper-limits are slightly lower than those of ϵ^{TR}_{TR}.

The shell model values for M_α, with $\alpha = GTq,\ Fq,\ Tq,\ GT\omega,\ F\omega,\ P,\ R,\ GT',\ T',\ GT\pi\nu,\ T\pi\nu$, are shown in Table XVI of the Appendix.

C. The short-range LNV couplings

Similar to the case of the long-range component, we extract the "on-axis" values of the short-range LNV parameters using the following expression for the half-life corresponding to the diagram of Fig. 1d:

$$\left[T^{0\nu}_{1/2}\right]^{-1} = g_A^4 \left[\left|\varepsilon^\beta_\alpha\right|^2 \mathcal{M}^2_{\alpha\beta}\right], \tag{13}$$

with $\varepsilon^\beta_\alpha = \{\varepsilon_1,\ \varepsilon_2,\ \varepsilon_3^{LLz(RRz)},\ \varepsilon_3^{LRz(RLz)},\ \varepsilon_4,\ \varepsilon_6\}$. The index $\beta = xyz$, with $xyz = L/R, L/R, L/R$, indicates the chirality of the hadronic and the leptonic currents. It is only possible to distinguish between the different chiralities in the case of ε_3 where we denote them explicitly as $\varepsilon_3^{LLz(RRz)}$ and $\varepsilon_3^{LRz(RLz)}$. For the other cases we omit this labeling.

Adapting the formalism of Ref. [22, 23, 82], we can write the coefficients containing combinations of NME and PSF as:

$$\mathcal{M}^2_1 = G_{01}\left[\left(\frac{F_S^{(3)}}{g_A}\right)^2 M_{FN}\right]^2, \tag{14a}$$

$$\mathcal{M}^2_2 = G_{01}\left[8\left(\frac{T_1^{(3)}}{g_A}\right)^2 M_{GTN}\right]^2, \tag{14b}$$

$$\begin{aligned}\mathcal{M}^2_{3LLz} &= \mathcal{M}^2_{3RRz} \\ &= G_{01}\left[M_{GTN} - \left(\frac{g_V}{g_A}\right)^2 M_{FN}\right]^2,\end{aligned} \tag{14c}$$

$$\begin{aligned}\mathcal{M}^2_{3LRz} &= \mathcal{M}^2_{3RLz} \\ &= G_{01}\left[M_{GTN} + \left(\frac{g_V}{g_A}\right)^2 M_{FN}\right]^2,\end{aligned} \tag{14d}$$

$$\mathcal{M}^2_4 = G_{09}\frac{(m_e R)^2}{8}\left[\frac{T_1^{(3)}}{g_A} M_{GTN}\right]^2, \tag{14e}$$

$$\mathcal{M}^2_5 = G_{09}\frac{(m_e R)^2}{8}\left[\frac{F_S^{(3)} g_V}{g_A^2} M_{FN}\right]^2. \tag{14f}$$

TABLE IV. The $\mathcal{M}^2_{\alpha\beta}$ values for the long-range part of the $0\nu\beta\beta$ decay process.

	^{48}Ca	^{76}Ge	^{82}Se	^{130}Te	^{136}Xe
$10^9\times\mathcal{M}^2_{V+A/V-A}$	1.45	1.40	5.11	3.67	3.09
$10^{13}\times\mathcal{M}^2_{V+A/V+A}$	1.09	0.39	3.21	1.11	0.89
$10^{10}\times\mathcal{M}^2_{S+P/S\pm P}$	8.85	1.33	5.11	2.72	2.15
$10^8\times\mathcal{M}^2_{TR/TR}$	0.25	1.09	4.04	3.28	2.79
$10^{10}\times\mathcal{M}^2_{\pi\nu}$	2.84	2.62	10.2	4.85	4.13

TABLE V. The "on-axis" values of the long-range LNV parameters ϵ^β_α. The last two lines present $\eta_{\pi\nu}$ and its corresponding $\tilde{\epsilon}^{TR}_{TR}$ limit.

	^{48}Ca	^{76}Ge	^{82}Se	^{130}Te	^{136}Xe
$\left\|\epsilon^{V+A}_{V-A}\right\|$	1.2×10^{-7}	1.9×10^{-9}	1.7×10^{-8}	5.1×10^{-9}	1.1×10^{-9}
$\left\|\epsilon^{V+A}_{V+A}\right\|$	1.3×10^{-5}	3.5×10^{-7}	2.2×10^{-6}	9.3×10^{-7}	2.0×10^{-7}
$\left\|\epsilon^{S+P}_{S\pm P}\right\|$	1.5×10^{-7}	6.0×10^{-9}	5.5×10^{-8}	1.9×10^{-8}	4.1×10^{-9}
$\left\|\epsilon^{TR}_{TR}\right\|$	8.8×10^{-8}	6.6×10^{-10}	6.2×10^{-9}	1.7×10^{-9}	3.6×10^{-10}
$\left\|\eta_{\pi\nu}\right\|$	4.3×10^{-9}	4.3×10^{-9}	3.9×10^{-8}	1.4×10^{-8}	2.9×10^{-9}
$\left\|\tilde{\epsilon}^{TR}_{TR}\right\|$	3.3×10^{-8}	5.4×10^{-10}	4.8×10^{-9}	1.8×10^{-9}	3.7×10^{-10}

TABLE VI. The $\mathcal{M}^2_{\alpha\beta}$ values for the short-range LNV parameters.

	^{48}Ca	^{76}Ge	^{82}Se	^{130}Te	^{136}Xe
$10^{13}\times\mathcal{M}^2_1$	2.63	1.83	6.86	4.83	4.03
$10^8\times\ \mathcal{M}^2_2$	0.68	0.50	1.87	1.34	1.11
$10^{10}\times\mathcal{M}^2_{3LLz(RRz)}$	1.20	0.87	3.26	2.33	1.93
$10^{11}\times\mathcal{M}^2_{3LRz(RLz)}$	4.27	3.16	11.8	8.50	7.03
$10^{10}\times\mathcal{M}^2_4$	0.91	0.70	2.50	1.74	1.44
$10^{12}\times\mathcal{M}^2_5$	1.15	0.84	3.01	2.06	1.72
$10^{10}\times\mathcal{M}^2_{\pi N}$	6.44	3.99	15.6	8.43	7.14

The parameters $F_S^{(3)} = 0.48$ and $T_1^{(3)} = 1.38$ are taken form Ref. [95]. The values of these $\mathcal{M}^2_{\alpha\beta}$ are presented in Table VI. Detailed expressions for M_{GTN} and M_{FN} are presented in the Appendix, and their shell model values are shown in Table XVII.

Considering the $0\nu\beta\beta$ amplitudes displayed in Figs. 2f and 2g in the one-pion and two-pion exchange modes it is possible to get alternative limits for ε_1 and ε_2 considering a different coefficient, $\mathcal{M}_{\pi N}$. The analysis of Ref. [88] suggests these alternative values, here denoted by $\tilde{\varepsilon}_1$ and $\tilde{\varepsilon}_2$, can be obtained as $\tilde{\varepsilon}_1 = \frac{64}{16}\eta_{\pi N}$, and $\tilde{\varepsilon}_2 = \frac{2}{3}\eta_{\pi N}$, using

$$\left[T^{0\nu}_{1/2}\right]^{-1} = g_A^4\left[\left|\eta_{\pi N}\right|^2 \mathcal{M}^2_{\pi N}\right], \tag{15}$$

where

$$\begin{aligned}\mathcal{M}^2_{\pi N} = G_{01}\big[&c^{1\pi}\left(M_{GT1\pi} + M_{T1\pi}\right) \\ &+ c^{2\pi}\left(M_{GT2\pi} + M_{T2\pi}\right)\big]^2.\end{aligned} \tag{16}$$

The expressions for the factors $c^{1\pi}$ and $c^{2\pi}$ are found in Eq. (151) of Ref. [82]. These factors depend on the masses of the up and down quark, and choosing $(m_u + m_d) = 11.6$ MeV [31, 96], one gets $c^{1\pi} = -83.598$, $c^{2\pi} = 359.436$ that we use in these calculations. The description of M_α (with $\alpha = GT1\pi,\ T1\pi,\ GT2\pi,\ T2\pi$) is presented in the Appendix.

Shown in Table VII are the values of the short-range LNV parameters. Using the different hadronization presented in Figs. 2f and 2g, $\tilde{\varepsilon}_1$ provides significantly more stringent upper-limits than ε_1. The $\tilde{\varepsilon}_2$ upper-limits are almost double those of ε_2, and therefore, we conclude that ε_2 are better constrained.

TABLE VII. The "on-axis" values of the short-range LNV parameters ε_α^β. The last three lines present the $\eta_{\pi N}$ limits for $\mathcal{R}_p$ SUSY, and their corresponding $\tilde{\varepsilon}_1$ and $\tilde{\varepsilon}_1$ limits, respectively.

	^{48}Ca	^{76}Ge	^{82}Se	^{130}Te	^{136}Xe
$\lvert\varepsilon_1\rvert$	8.6×10^{-6}	1.6×10^{-7}	1.5×10^{-6}	4.6×10^{-7}	9.3×10^{-8}
$\lvert\varepsilon_2\rvert$	5.3×10^{-8}	9.8×10^{-10}	9.1×10^{-9}	2.7×10^{-9}	5.7×10^{-10}
$\lvert\varepsilon_3^{LLz(RRz)}\rvert$	4.0×10^{-7}	7.4×10^{-9}	6.9×10^{-8}	2.0×10^{-8}	4.3×10^{-9}
$\lvert\varepsilon_3^{LRz(RLz)}\rvert$	6.7×10^{-7}	1.2×10^{-8}	1.1×10^{-7}	3.4×10^{-8}	7.1×10^{-9}
$\lvert\varepsilon_4\rvert$	4.6×10^{-7}	8.3×10^{-9}	7.8×10^{-8}	2.4×10^{-8}	5.0×10^{-9}
$\lvert\varepsilon_5\rvert$	4.1×10^{-6}	7.6×10^{-8}	7.1×10^{-7}	2.2×10^{-7}	4.6×10^{-8}
$\lvert\eta_{\pi N}\rvert$	1.7×10^{-7}	3.5×10^{-9}	3.1×10^{-8}	1.1×10^{-8}	2.2×10^{-9}
$\lvert\tilde{\varepsilon}_1\rvert$	6.9×10^{-7}	1.4×10^{-8}	1.3×10^{-7}	4.3×10^{-8}	9.0×10^{-9}
$\lvert\tilde{\varepsilon}_2\rvert$	1.2×10^{-7}	2.3×10^{-9}	2.1×10^{-8}	7.1×10^{-9}	1.5×10^{-9}

The expression for the $\mathcal{M}^2_{\pi N}$ contains the $c^{1\pi}$ and $c^{2\pi}$ parameters, which carry information from the hadronization procedure. The two terms in Eq. (16) contribute with similar strength, but as mentioned before, the hadronization procedure used here does not provide reliable relative phases of the $c^{1\pi}$ and $c^{2\pi}$ parameters. Therefore, the values of $\tilde{\varepsilon}_1$ and $\tilde{\varepsilon}_2$ extracted in Table VII may be uncertain. Fortunately, there are no othe NME/parameters affected by relative phases, and in addition, these two values don't influence the analysis of the scale of the BSM physics given in the next section.

V. ANALYSIS OF NEUTRINOLESS DOUBLE-BETA DECAY HALF-LIFE RATIOS

Under the assumption that a single mechanism/coupling dominates, we can reduce the expression of the half-life for all 12 mechanisms to the following form :

$$\left[T^{0\nu}_{1/2}\right]^{-1} = g_A^4 \left|\eta_{LNV}\right|^2 \mathcal{M}^2_{LNV}, \tag{17}$$

where, similar to Eq. (5), $g_A = 1.27$ is the axial-vector coupling constant, η_{LNV} represents the effective LNV parameter, while the $\mathcal{M}^2_{LNV}$ coefficient contains the combination of NME and PFS associated to the LNV parameter. For example, in the case of the heavy neutrino exchange mechanism $\mathcal{M}^2_{0N} = {g_A}^4|\eta_0\nu|^2 G_{01} {M_{0N}}^2$. Using this equation is particularly useful in predicting the experimental sensitivity of different isotopes with respect to certain $0\nu\beta\beta$ mechanisms.

The current best experimental $0\nu\beta\beta$ half-life limit is provided by the KamLand-Zen Collaboration $T^{1/2}_{^{136}\mathrm{Xe}} = 1.07\times10^{26}$ [72]. Based on this limit, we extract on-axis the η_{LNV} effective LNV parameters of interest for ^{136}Xe.

Equation (17) is factorized in such a way that the half-life ratio of two isotopes, or even between different mechanisms assumed to dominate the transition in the same isotope, can be easily obtained simply from the inverse of the $\mathcal{M}^2_{LNV}$ ratio. This eliminates the need to rely on any experimental half-life limit, or extracted LNV parameters for evaluating the relative sensitivity of different isotopes to various mechanisms. We present our analysis and results from two perspectives: on one side, we evaluate the equivalent half-lives required to match the current ^{136}Xe sensitivity to the LNV parameters, and on the other side, we search for the best half-life ratios that are expected to help distinguish between the different possible contributions to the decay rate, under the one mechanism/coupling dominance assumption.

We calculate the NME components of the $\mathcal{M}^2_{LNV}$ coefficients within the interacting shell model (ISM). For each of the isotopes we obtain results using two sets of effective Hamiltonians, denoted as "CMU" and "St-Ma", which are popular in the literature and have been thoroughly tested against experimental data. Their description is given in the Introduction. All the NME used in this analysis were calculated using a Jastrow short-range correlation (SRC) method using the CD-Bonn and AV-18 parametrizations (see e.g. Ref. [36] and Refs. therein). Different choices for the method of including the SRC affect the values of the NME, as has been discussed in many papers in recent literature. One can find a graphical representation of these effects on the NME in Fig. 6 and Fig. 7 of Ref. [45] for the light left-handed neutrino exchange and for the heavy right-handed neutrino exchange, respectively. Although the differences in NME values can be large, in the case of shell model calculations, the ratio of $\mathcal{M}^2_{LNV}$ coefficients are usually stable when calculated consistently with the same parametrization. This behavior is detailed in the following subsections.

The PSF components are calculated using a recently proposed effective method described in great detail in Ref. [81]. G_{01} values were calculated with a screening factor (s_f) of 94.5, while for $G_{02} - G_{09}$ we used $s_f = 92.0$ that was shown to provide results very close to those of Ref. [84].

A. Calculated half-lives for ^{48}Ca, ^{76}Ge, ^{82}Se, and ^{130}Te expected to match the current ^{136}Xe sensitivity

In this subsection we extract the LNV parameters from the current ^{136}Xe experimental limit of 1.07×10^{26} years [72]. We take into account two SRC parameterizations (CD-Bonn and AV-18) and two sets of effective Hamiltonians. The values of the LNV parameters are shown in the upper parts of all the Tables VIII - XIII as η_{LNV}. The upper limits of η_{LNV} extracted from the present lower limit of the ^{136}Xe half-life using calculations done with CMU Hamiltonians and CD-Bonn SRC are repeated from Tables II, V and VII, while those extracted using matrix elements calculated with AV-18 SRC or/and St-Ma Hamiltonians are displayed in these tables for the first time. For consistency and an easier comparison, the $\mathcal{M}^2_{LNV}$ coefficients calculated with CD-Bonn SRC and CMU Hamiltonians in Tables X and XII are repeated from Tables IV and IV. All the other $\mathcal{M}^2_{LNV}$ coefficients

presented in the Tables VIII - XIII are new. We use these parameters together with shell model NME to predict the half-life limits of ^{48}Ca, ^{76}Ge, ^{82}Se, and ^{130}Te that are needed to match the current limit for ^{136}Xe for each of the LNV mechanisms. This could prove particularly useful in determining the minimum required isotope quantities needed by the experiments in order to obtain better constraints on the LNV parameters. This information will, however, need to be adjusted to the particular setup of each experiment and correlated with their detection efficiency of $0\nu\beta\beta$ transitions for their isotopes of choice.

Table VIII presents upper-limit values of the η_α LNV parameters for the LRSM and $\mathcal{R}_p$ extracted on-axis from the most recent ^{136}Xe experiment [72], the CMU $\mathcal{M}^2_{LNV}$ coefficients containing NME and PSF, and the calculated half-life limits for the other isotopes of experimental interest predicted when taking into account the ^{136}Xe η_α LNV parameters. The effect of the SRC parameterizations on the different NME can be easily seen in this table. The $\mathcal{M}^2_{LNV}$ coefficients can almost double when changing from AV-18 to CD-Bonn in the case of $\mathcal{M}^2_{0N}$. Nevertheless, the predicted half-life limits are very stable if the extracted ^{136}Xe LNV parameters are chosen from calculations with the same SRC.

Using the St-Ma effective Hamiltonians, in Table IX we recalculate the quantities from Table VIII. The same observations related to the SRC are valid also in this case. The most significant $\mathcal{M}^2_{LNV}$ change occurs for the $\mathcal{M}^2_{0N}$ coefficient, but the predicted half-life limits remain stable. Regarding how the effective Hamiltonians affect the NME, one can see that KB3G preferred by St-Ma provides higher values for ^{48}Ca than GXPF1A preferred by us (CMU), GCN.28-50 yields lower NME than JUN45 for ^{76}Ge and ^{82}Se, and GCN.50:82 results in higher NME than SVD for ^{130}Te and ^{136}Xe.

Within the framework of the EFT, in Table X we investigate the $\mathcal{M}^2_{LNV}$ coefficients, and the half-lives corresponding to the dimension 6 Lagrangian in Eq. (2).

In this case, the $|\epsilon^{V+A}_{V-A}|$ LNV parameters, the $\mathcal{M}^2_{V+A/V-A}$ coefficients, and the $T_{V+A/V-A}$ half-lives of the EFT also correspond to the so-called "$\eta-$mechanism" in the LRSM and presented in Table VIII. Similarly the $|\epsilon^{V+A}_{V+A}|$ LNV parameters, the $\mathcal{M}^2_{V+A/V+A}$ coefficients, the $T_{V+A/V+A}$ half-lives, correspond the so-called "$\lambda-$mechanism". One can obtain another alternative value for $|\epsilon^{TR}_{TR}|$, $|\tilde{\epsilon}^{TR}_{TR}| = |\eta_{\pi\nu}|/8$, where our $\eta_{\pi\nu}$ plays the same role as $\eta^{11}_{(q)LR}$ in Eq.(22) of Ref. [78] and $\eta_{\bar{q}}$ in Table VIII (see also Eq. (154) of Ref. [82]). Here, we notice a significant effect of the SRC choice on the NME, but also on the predicted half-life limits, especially in the case of ^{48}Ca. The ^{136}Xe alternative $|\tilde{\epsilon}^{TR}_{TR}| = |\eta_{\pi\nu}|/8$ LNV parameter is similar to $|\epsilon^{TR}_{TR}|$, but the associated NME and half-life limits are very stable with respect to the choice of SRC.

For the second set of Hamiltonians, we present the results corresponding to the dimension 6 Lagrangian of Eq. (2) in Table XI. The same conclusions and observations that we made for Table X are also valid here.

The results corresponding to the dimension 9 Lagrangian of Eq. (3) are displayed in Table XII as in the previous tables. Regarding $|\varepsilon_3^{RRz(LLz)}|$, we note that the results closely correspond to the ones for $|\eta_{0N}|$ in Table VIII for the LRSM, but the tensor component of the NME is missing in the formalism associated to this case. The NME that enter the $\mathcal{M}^2_{LNV}$ coefficients manifest the same behavior as the $\mathcal{M}^2_{0N}$ when changing SRC parameterizations, but the predicted half-life limits are very stable.

Finally, we show our results corresponding to the dimension 9 Lagrangian of Eq. (3) when using the second set of Hamiltonians in Table XIII. The dependence of the $\mathcal{M}^2_{LNV}$ coefficients and of the predicted half-life limits is similar to that found in Table XII.

B. Disentangling contributions to the $0\nu\beta\beta$ decay rate from half-life ratios

The analysis is based on choosing a pair of isotopes, calculating the ratio of half-lives for different mechanisms, and identifying results that stand out and do not overlap. This means that we use the figures to search for bars that have a noticeable gap between them and other higher or lower bars. Quite obviously, the lower values could also be important and one could inverse the ratio to better see the gap between them and other results.

One can easily notice in the following figures and in the tables of the previous subsection that the $\mathcal{M}^2_{LNV}$ coefficients of ^{130}Te are very close to those of ^{136}Xe. This feature can be understood as due to the similar $Q_{\beta\beta}$ values of these two isotopes leading to similar PSF, and due to the fact that in the same valence space the NME is changing very slowly with the mass A when the same effective Hamiltonian is used. The main consequence of this fact is that both half-lives are of the same order. Due to this resemblance, measuring any of these two nuclei is equally desirable as they can easily substitute each other in the analysis of half-lives. The downside of this feature is that the half-life ratio among themselves cannot provide us with information that would enable one to distinguish different contributions to the $0\nu\beta\beta$ rate. Although the predicted half-life for ^{130}Te is slightly lower than that of ^{136}Xe, and this could be favorable in some of the half-life ratios, the current experimental limits and trends lead us to believe that ^{136}Xe and ^{76}Ge are likely to be the first ones to be experimentally measured. Based on this assumption about the experimental expectations, we present our analysis in relation to these two isotopes. The reader can, however, use the calculated $\mathcal{M}^2_{LNV}$ coefficients listed in the tables of the previous Subsection to investigate the half-life ratios of any pairs of nuclei.

In Fig. 3 we present the half-life ratio of ^{136}Xe over another isotope for the mechanisms discussed, in the case of our preference of Hamiltonians (CMU). The bars connect

TABLE VIII. The upper part presents the η_α LNV parameters for the LRSM and SUSY extracted on-axis from the most recent ^{136}Xe experiment [72], the middle part shows our shell model $\mathcal{M}^2_{LNV}$ coefficients containing NME and PSF, and the lower part lists the calculated half-life limits in years for the isotopes of experimental interest predicted when taking into account the ^{136}Xe LNV parameters. The NME are calculated with the CMU effective Hamiltonians and two SRC parameterizations: CD-Bonn and AV-18.

SRC	η_{LNV}	$\lvert\eta_{0\nu}\rvert \times 10^7$	$\lvert\eta_{0N}\rvert \times 10^9$	$\lvert\eta_{\lambda}\rvert \times 10^7$	$\lvert\eta_{\eta}\rvert \times 10^9$	$\lvert\eta_{\tilde{q}}\rvert \times 10^9$	$\lvert\eta_{\lambda'}\rvert \times 10^9$
CD-Bonn		2.84	4.40	2.01	1.08	2.95	2.24
AV-18		3.08	6.11	2.17	1.31	3.10	2.12
	$\mathcal{M}^2_{LNV}$	$\mathcal{M}^2_{0\nu} \times 10^{14}$	$\mathcal{M}^2_{0N} \times 10^{10}$	$\mathcal{M}^2_{\lambda} \times 10^{13}$	$\mathcal{M}^2_{\eta} \times 10^{9}$	$\mathcal{M}^2_{\tilde{q}} \times 10^{10}$	$\mathcal{M}^2_{\lambda'} \times 10^{10}$
CD-Bonn	^{48}Ca	2.57	1.63	1.09	1.45	2.83	6.44
	^{76}Ge	3.00	0.87	0.39	1.40	2.62	3.99
	^{82}Se	11.5	3.28	3.21	5.11	10.20	15.6
	^{130}Te	5.22	2.25	1.11	3.67	4.85	8.43
	^{136}Xe	4.40	1.86	0.89	3.09	4.13	7.14
AV-18	^{48}Ca	2.19	0.94	0.90	0.92	2.57	7.08
	^{76}Ge	2.67	0.46	0.34	0.95	2.41	4.40
	^{82}Se	10.3	1.75	2.85	3.47	9.43	17.1
	^{130}Te	4.49	1.17	0.96	2.48	4.38	9.43
	^{136}Xe	3.79	0.96	0.77	2.10	3.73	7.97
	$T_{LNV} \times 10^{-26}$	$T_{0\nu}$	T_{0N}	T_{λ}	T_{η}	$T_{\tilde{q}}$	$T_{\lambda'}$
CD-Bonn	^{48}Ca	1.83	1.22	0.87	2.28	1.56	1.19
	^{76}Ge	1.57	2.28	2.45	2.36	1.69	1.92
	^{82}Se	0.41	0.61	0.30	0.65	0.43	0.49
	^{130}Te	0.90	0.88	0.85	0.90	0.91	0.91
AV-18	^{48}Ca	1.85	1.09	0.91	2.45	1.55	1.20
	^{76}Ge	1.52	2.22	2.39	2.37	1.66	1.94
	^{82}Se	0.39	0.59	0.29	0.65	0.42	0.50
	^{130}Te	0.90	0.88	0.86	0.90	0.91	0.90

two values for each ratio. One value is obtained using the CD-Bonn parametrization for the SRC, while the other value is the result of our calculations using the AV-18 parametrization. The graphical representation emphasizes the impact of the choice of SRC for the ratio of the half-lives. It is easy to notice that for most cases, the SRC plays an insignificant role for the half-life ratios, and the bars of the plots had to be increased for the reader to see them. In the two cases where SRC did make a difference ($S+P/S\pm P$ and TR/TR), the bars are completely outside of the range of those provided by the other mechanisms, and the analysis is not affected by their spread. From this figure, it appears that the dominance of the $\epsilon^{S+P}_{S\pm P}$ and ϵ^{TR}_{TR} contributions could be confirmed or ruled out by the ^{136}Xe/^{48}Ca ratio, while the ϵ^{V+A}_{V+A} could be investigated by the ^{136}Xe/^{82}Se ratio. Then, the dominance of ϵ^{V+A}_{V-A} mechanism (known also as the η mechanism) could be identified from the two-electron angular and energy distributions [15, 16].

The same analysis performed in Fig. 3 is done for the St-Ma choice of Hamiltonians, and we present those results in Fig. 4. The y-axis ranges are kept identical for an easier observation of the effect of changing the shell model Hamiltonians. Different from the previous figure is that the ^{130}Te almost flat line has shifted higher, while the other ratios have decreased in magnitude. The $\epsilon^{S+P}_{S\pm P}$ and ϵ^{TR}_{TR} contributions can still be identifiable with the ^{136}Xe/^{48}Ca ratio, but the ϵ^{V+A}_{V+A} from ^{136}Xe/^{82}Se identification would be not as sensitive as for the CMU NME.

Similar to Fig. 3, we also represent in Fig. 5 the half-life ratios of ^{76}Ge over those of other isotopes to search for potentially other identifiable mechanisms. As in the previous cases, it is easy to see the consistency of results using the same SRC. Because both ^{76}Ge and ^{82}Se can be calculated with the same Hamiltonian, we consider the ratios of half-lives for these nuclei to be the ones with the least uncertainties. Due to this feature, the dominance of the ϵ^{V+A}_{V+A} contribution could be reliably validated or ruled-out with this pair of isotopes. Very similar to the previous two figures, the $\epsilon^{S+P}_{S\pm P}$ and ϵ^{TR}_{TR} contributions could also be confirmed or ruled out by the ^{76}Ge/^{48}Ca ratio.

As in Fig. 5, we show the results for the St-Ma Hamiltonians in Fig. 6 in the same y-axis range. From this image we could identify the ϵ^{V+A}_{V+A} contribution by the

TABLE IX. Same as Table VIII, but with $\mathcal{M}^2_{LNV}$ coefficients obtained using St-Ma Hamiltonians.

SRC	η_{LNV}	$\lvert\eta_{0\nu}\rvert \times 10^{-7}$	$\lvert\eta_{0N}\rvert \times 10^{-9}$	$\lvert\eta_{\lambda}\rvert \times 10^{-7}$	$\lvert\eta_{\eta}\rvert \times 10^{-9}$	$\lvert\eta_{\tilde{q}}\rvert \times 10^{-9}$	$\lvert\eta_{\lambda'}\rvert \times 10^{-9}$
CD-Bonn		2.09	3.14	1.62	0.82	2.19	1.61
AV-18		2.24	4.34	1.74	1.00	2.30	1.52
	$\mathcal{M}^2_{LNV}$	$\mathcal{M}^2_{0\nu} \times 10^{14}$	$\mathcal{M}^2_{0N} \times 10^{10}$	$\mathcal{M}^2_{\lambda} \times 10^{13}$	$\mathcal{M}^2_{\eta} \times 10^{9}$	$\mathcal{M}^2_{\tilde{q}} \times 10^{10}$	$\mathcal{M}^2_{\lambda'} \times 10^{10}$
CD-Bonn	^{48}Ca	3.13	1.91	1.48	1.80	3.19	7.43
	^{76}Ge	1.98	0.71	0.22	1.05	1.73	3.01
	^{82}Se	7.54	2.57	1.84	3.74	6.51	11.30
	^{130}Te	12.5	5.57	2.19	8.29	11.4	21.3
	^{136}Xe	8.22	3.64	1.38	5.35	7.47	13.9
AV-18	^{48}Ca	2.66	1.08	1.23	1.13	2.87	8.21
	^{76}Ge	1.75	0.38	0.19	0.70	1.58	3.33
	^{82}Se	6.68	1.37	1.62	2.52	5.97	12.5
	^{130}Te	10.8	2.92	1.89	5.58	10.3	23.8
	^{136}Xe	7.14	1.91	1.19	3.60	6.78	15.5
	$T_{LNV} \times 10^{-26}$	$T_{0\nu}$	T_{0N}	T_{λ}	T_{η}	$T_{\tilde{q}}$	$T_{\lambda'}$
CD-Bonn	^{48}Ca	2.81	2.04	1.00	3.17	2.51	2.01
	^{76}Ge	4.44	5.49	6.65	5.43	4.62	4.96
	^{82}Se	1.17	1.52	0.80	1.53	1.23	1.32
	^{130}Te	0.70	0.70	0.67	0.69	0.70	0.70
AV-18	^{48}Ca	2.87	1.90	1.03	3.41	2.52	2.03
	^{76}Ge	4.37	5.41	6.57	5.47	4.57	4.99
	^{82}Se	1.14	1.49	0.79	1.53	1.21	1.33
	^{130}Te	0.71	0.70	0.67	0.69	0.70	0.70

^{76}Ge/^{82}Se ratio, but the $\epsilon^{S+P}_{S\pm P}$ and ϵ^{TR}_{TR} mechanisms are more difficult to confirm or rule out than in the previous figure using the ^{76}Ge/^{48}Ca ratio.

One can notice that using different effective Hamiltonians can produce significant changes in the half-lives ratios, much more than changing the SRC and finite nucleon size parametrization. Previously, the effects of different effective shell model Hamiltonians on the neutrinoless half-lives have not been considered. Usually just one set of NME was taken into account. We emphasize that in the half-lives formulae the NME values are squared, thus making any significant change due to different effective Hamiltonian amplified in the ratios of the half-lives. These differences lead to large effects, which can be observed when comparing Fig. 5 with Fig. 6.

In all cases presented, the short-range contributions corresponding to the dimension 9 Lagrangian cannot be disentangled from each other using ratios of half-lives. In the Tables and in the Figures the results for these cases correspond to $|\varepsilon^{\beta}_{\alpha}|$. None of the half-lives, or the ratios of half-lives, are different enough to be distinguishable from the others.

VI. DISCUSSIONS

From the $\eta_{0\nu}$ limits presented in Table III for ^{136}Xe, one gets the lowest shell model upper-limit for the Majorana neutrino mass $\langle m_{\beta\beta}\rangle \sim 140$ meV. A wider range of values, $60 - 165$ meV can be found if the NME calculated with a larger number of nuclear models are considered [72].

Considering the diagram in Fig. 2e, it is possible to get lower limits for ϵ^{TR}_{TR}, denoted as $\tilde{\epsilon}^{TR}_{TR}$ in Table V, than those corresponding to the diagram in Fig. 2c, with the exception of ^{48}Ca, as can be seen in Table V. Considering the different hadronization scenario presented in Figs. 2f and 2g, $\tilde{\varepsilon}_1$ provides a significantly more stringent upper-limits than ε_1. The $\tilde{\varepsilon}_2$ upper-limits are almost double those of ε_2.

As suggested in Ref. [91] (see the diagrams of their Fig.1), at the electroweak scale when the appropriate Higgs fields are included, the diagram 1.b originates from a dimension-5 BSM Lagrangian, $\mathcal{O}_5$, responsible for the Majorana neutrino mass. Similarly the low-energy dimension-6 Lagrangian $\mathcal{L}_6$ corresponds to a dimension-7 BSM operator, $\mathcal{O}_7$, and the low energy dimension-9 Lagrangian $\mathcal{L}_9$ can be rearranged as dimension-9 and dimension-11 operators, $\mathcal{O}_9$ and $\mathcal{O}_{11}$. Using the effective field theory one can infer the energy scale Λ_D up to

TABLE X. Same as Table VIII, but for the long-range contribution to the $0\nu\beta\beta$ diagram, corresponding to the dimension 6 Lagrangian for the CMU set of Hamiltonians.

SRC	η_{LNV}	$\lvert\epsilon^{V+A}_{V-A}\rvert \times 10^9$	$\lvert\epsilon^{V+A}_{V+A}\rvert \times 10^7$	$\lvert\epsilon^{S+P}_{S\pm P}\rvert \times 10^9$	$\lvert\epsilon^{TR}_{TR}\rvert \times 10^{10}$	$\lvert\eta_{\pi\nu}\rvert \times 10^9$
CD-Bonn		1.08	2.01	4.09	3.59	2.95
AV-18		1.31	2.17	5.65	4.63	3.10
	$\mathcal{M}^2_{LNV}$	$\mathcal{M}^2_{V+A/V-A} \times 10^{14}$	$\mathcal{M}^2_{V+A/V+A} \times 10^{10}$	$\mathcal{M}^2_{S+P/S\pm P} \times 10^{10}$	$\mathcal{M}^2_{TR/TR} \times 10^8$	$\mathcal{M}^2_{\pi\nu} \times 10^{10}$
CD-Bonn	^{48}Ca	1.45	1.09	8.85	0.25	2.83
	^{76}Ge	1.40	0.39	1.33	1.09	2.62
	^{82}Se	5.11	3.21	5.12	4.04	10.2
	^{130}Te	3.67	1.11	2.72	3.28	4.85
	^{136}Xe	3.09	0.89	2.15	2.79	4.13
AV-18	^{48}Ca	0.92	0.90	7.03	0.04	2.57
	^{76}Ge	0.95	0.34	0.78	0.63	2.41
	^{82}Se	3.47	2.85	3.05	2.34	9.43
	^{130}Te	2.48	0.96	1.45	1.96	4.38
	^{136}Xe	2.10	0.77	1.13	1.67	3.73
	$T_{LNV} \times 10^{-26}$	$T_{V+A/V-A}$	$T_{V+A/V+A}$	$T_{S+P/S\pm P}$	$T_{TR/TR}$	$T_{\pi\nu}$
CD-Bonn	^{48}Ca	2.28	0.87	0.26	12.0	1.56
	^{76}Ge	2.36	2.45	1.73	2.74	1.69
	^{82}Se	0.65	0.30	0.45	0.74	0.43
	^{130}Te	0.90	0.85	0.85	0.91	0.91
AV-18	^{48}Ca	2.45	0.91	0.17	45.1	1.55
	^{76}Ge	2.37	2.39	1.54	2.83	1.66
	^{82}Se	0.65	0.29	0.40	0.76	0.42
	^{130}Te	0.90	0.86	0.83	0.91	0.91

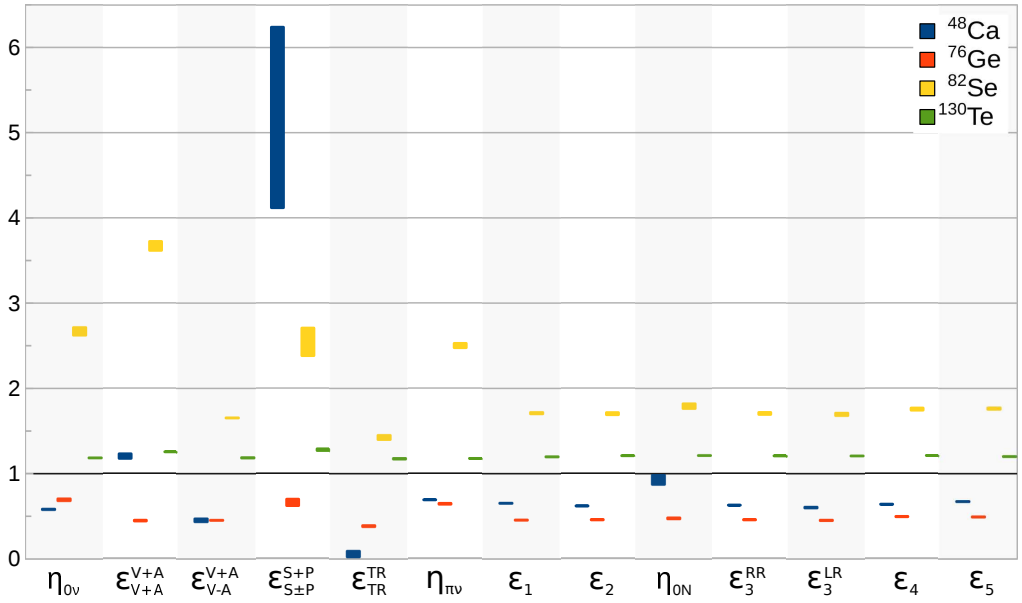

FIG. 3. The ratio between the ^{136}Xe half-life and the T_α half-lives of several experimentally interesting isotopes, in the case of 12 EFT LNV couplings plus η_{0N}. The left to right order of the bars corresponds to up to down order in the Legend. The height of the bars represents the difference between results obtained with different SRC parameterizations. η_{0N} plays a similar role to $\varepsilon_3^{RRz(LLz)}$.

TABLE XI. Same as Table X, but with $\mathcal{M}^2_{LNV}$ coefficients calculated with St-Ma Hamiltonians.

SRC	η_{LNV}	$\lvert\epsilon^{V+A}_{V-A}\rvert \times 10^9$	$\lvert\epsilon^{V+A}_{V+A}\rvert \times 10^7$	$\lvert\epsilon^{S+P}_{S\pm P}\rvert \times 10^9$	$\lvert\epsilon^{TR}_{TR}\rvert \times 10^{10}$	$\lvert\eta_{\pi\nu}\rvert \times 10^9$
CD-Bonn		0.82	1.62	2.86	2.80	2.19
AV-18		1.00	1.74	3.87	3.67	2.30
	$\mathcal{M}^2_{LNV}$	$\mathcal{M}^2_{V+A/V-A} \times 10^{14}$	$\mathcal{M}^2_{V+A/V+A} \times 10^{10}$	$\mathcal{M}^2_{S+P/S\pm P} \times 10^{10}$	$\mathcal{M}^2_{TR/TR} \times 10^8$	$\mathcal{M}^2_{\pi\nu} \times 10^{10}$
CD-Bonn	^{48}Ca	1.80	1.48	7.50	0.73	3.19
	^{76}Ge	1.05	0.22	1.03	0.81	1.73
	^{82}Se	3.74	1.84	3.63	3.01	6.51
	^{130}Te	8.29	2.19	6.65	7.09	11.40
	^{136}Xe	5.35	1.38	4.39	4.58	7.47
AV-18	^{48}Ca	1.13	1.23	5.63	0.26	2.87
	^{76}Ge	0.70	0.19	0.61	0.46	1.58
	^{82}Se	2.52	1.62	2.11	1.73	5.97
	^{130}Te	5.58	1.89	3.61	4.13	10.30
	^{136}Xe	3.60	1.19	2.40	2.66	6.78
	$T_{LNV} \times 10^{-26}$	$T_{V+A/V-A}$	$T_{V+A/V+A}$	$T_{S+P/S\pm P}$	$T_{TR/TR}$	$T_{\pi\nu}$
CD-Bonn	^{48}Ca	3.17	1.00	0.63	6.74	2.51
	^{76}Ge	5.43	6.65	4.55	6.03	4.62
	^{82}Se	1.53	0.80	1.29	1.63	1.23
	^{130}Te	0.69	0.67	0.71	0.69	0.70
AV-18	^{48}Ca	3.41	1.03	0.46	10.80	2.52
	^{76}Ge	5.47	6.57	4.23	6.15	4.57
	^{82}Se	1.53	0.79	1.21	1.64	1.21
	^{130}Te	0.69	0.67	0.71	0.69	0.70

which these effective field operators are not broken:

$$\mathcal{L}_D = \frac{g}{(\Lambda_D)^{D-4}}\mathcal{O}_D, \tag{18}$$

where D is the dimension of the effective field operator. Here g is considered to be a dimensionless coupling constant of the order of 1. Following Ref. [91] one can find relations between the constants entering our $\mathcal{L}_6$ and $\mathcal{L}_9$ Lagrangian and the effective field theory Lagrangians above the electroweak scale, Eq. (18).

$$m_e\bar{\epsilon}_5 = \frac{g^2(yv)^2}{\Lambda_5}, \qquad \frac{G_F\bar{\epsilon}_7}{\sqrt{2}} = \frac{g^3(yv)}{2(\Lambda_7)^3},$$
$$\frac{G_F^2\bar{\epsilon}_9}{2m_p} = \frac{g^4}{(\Lambda_9)^5}, \qquad \frac{G_F^2\bar{\epsilon}_{11}}{2m_p} = \frac{g^6(yv)^2}{(\Lambda_{11})^7}. \tag{19}$$

Here, $m_e = 0.511 \times 10^{-3}$ GeV is the electron mass, $g = 1$ is a generic coupling constant, $v = 174$ GeV is the Higgs vacuum expectation value, y is a Yukawa coupling associated to the interaction with the Higgs bosons, $G_F = 1.166\times10^{-5}$ GeV^{-2} is the Fermi coupling constant, and $m_p = 0.938$ GeV is the proton mass. The $\bar{\epsilon}_D$ (with $D = \{5,\ 7,\ 9,\ 11\}$) can be extracted from the LNV parameters in Eqs. (2) and (3). Considering that values of these LNV parameters may be affected by mixing angles that might distort the scales in Eq. (18), we choose their maximum values: $\bar{\epsilon}_5 = |\eta_{0\nu}|$, $\bar{\epsilon}_7 = \mathrm{Max}\Big[|\epsilon^{V+A}_{V-A}|, |\epsilon^{V+A}_{V+A}|, |\epsilon^{S+P}_{S\pm P}|, |\epsilon^{TR}_{TR}|\Big]$, $\bar{\epsilon}_9 = \mathrm{Max}\Big[|\varepsilon_1|, |\varepsilon_2|, |\varepsilon_3^{LLz(RRz)}|, |\varepsilon_3^{LRz(RLz)}|, |\varepsilon_4|, |\varepsilon_5|\Big]$, and $\bar{\epsilon}_{11} = \bar{\epsilon}_9$.

To extract the limits of the BSM scales $\Lambda_{5,7,9,11}$ we need the most stringent limits for the LNV parameters, which are found for the case of ^{136}Xe. Inspecting Tables V and VII we found that $\bar{\epsilon}_5$ corresponds to the $\eta_{0\nu}$ parameter of the light left-handed Majorana neutrino exchange mechanism. For $\bar{\epsilon}_7$ we choose ϵ^{V+A}_{V+A}, that is the largest long-range $\epsilon^{\beta}_{\alpha}$ parameter. In the case of $\bar{\epsilon}_9 = \bar{\epsilon}_{11}$ we select ε_1, being the largest short-range $\varepsilon^{\beta}_{\alpha}$ parameter. These values are listed in Table XIV.

As in Ref. [91] we take $g = 1$ in Eq. (18). However, we introduce here the Yukawa coupling y between the Higgs boson field and the fermion fields, and we consider two cases: (i) $y = 1$ corresponding to the top quark mass (choice made in Ref. [91]), and (ii) $y = 3 \times 10^{-6}$ corresponding to the electron mass. Based on these values we calculate the limits of the new BSM scales or different dimension-D operators. The results are shown in Table XIV. The Λ^0_D scales are calculated using the present lower limit for the half-life of ^{136}Xe, 1.1×10^{26}. Λ_D is estimated assuming a half-life of $T_{1/2} \approx 1.1 \times 10^{28}$ years, which would correspond to a $\langle m_{\beta\beta}\rangle \approx 14$ meV.

The Λ_9 scale does not depend on the unknown Yukawa

TABLE XII. Same as Tables VIII and X, for the short-range contribution to the $0\nu\beta\beta$ diagram, corresponding to the dimension 9 Lagrangian for the CMU set of Hamiltonians.

SRC	η_{LNV}	$\lvert\varepsilon_1\rvert \times 10^8$	$\lvert\varepsilon_2\rvert \times 10^{10}$	$\lvert\varepsilon_3^{RRz(LLz)}\rvert \times 10^9$	$\lvert\varepsilon_3^{LRz(RLz)}\rvert \times 10^9$	$\lvert\varepsilon_4\rvert \times 10^9$	$\lvert\varepsilon_5\rvert \times 10^8$	$\lvert\eta_{\pi N}\rvert \times 10^9$
CD-Bonn		9.44	5.70	4.31	7.15	5.00	4.58	2.24
AV-18		11.4	8.14	5.95	10.9	7.15	5.52	2.12
	$\mathcal{M}^2_{LNV}$	$\mathcal{M}^2_1 \times 10^{13}$	$\mathcal{M}^2_2 \times 10^8$	$\mathcal{M}^2_{3/LLz(RRz)} \times 10^{10}$	$\mathcal{M}^2_{3/LRz(RLz)} \times 10^{11}$	$\mathcal{M}^2_4 \times 10^{10}$	$\mathcal{M}^2_5 \times 10^{12}$	$\mathcal{M}^2_{\pi N} \times 10^{10}$
CD-Bonn	^{48}Ca	2.63	0.68	1.21	4.27	0.91	1.15	6.44
	^{76}Ge	1.83	0.50	0.87	3.16	0.70	0.84	3.99
	^{82}Se	6.86	1.87	3.26	11.8	2.50	3.01	15.6
	^{130}Te	4.83	1.34	2.33	8.50	1.74	2.06	8.43
	^{136}Xe	4.03	1.11	1.93	7.03	1.44	1.71	7.14
AV-18	^{48}Ca	1.81	0.33	0.63	1.81	0.44	0.80	7.08
	^{76}Ge	1.27	0.25	0.46	1.38	0.35	0.58	4.40
	^{82}Se	4.77	0.93	1.74	5.19	1.24	2.09	17.1
	^{130}Te	3.32	0.65	1.22	3.66	0.85	1.41	9.43
	^{136}Xe	2.77	0.54	1.02	3.03	0.70	1.18	7.97
	$T_{LNV} \times 10^{-26}$	T_1	T_2	$T_{3/RRz(LLz)}$	$T_{3/LRz(RLz)}$	T_4	T_5	$T_{\pi N}$
CD-Bonn	^{48}Ca	1.64	1.73	1.71	1.76	1.68	1.59	1.19
	^{76}Ge	2.36	2.38	2.38	2.38	2.20	2.18	1.92
	^{82}Se	0.63	0.63	0.63	0.64	0.62	0.61	0.49
	^{130}Te	0.89	0.89	0.89	0.89	0.88	0.89	0.91
AV-18	^{48}Ca	1.64	1.74	1.72	1.79	1.69	1.59	1.20
	^{76}Ge	2.35	2.35	2.35	2.35	2.17	2.17	1.94
	^{82}Se	0.62	0.62	0.62	0.63	0.61	0.60	0.50
	^{130}Te	0.89	0.89	0.89	0.89	0.89	0.89	0.90

coupling, and from that point of view, if $\mathcal{O}_9$ amplitude is dominant, that would indicate that the scale of new physics should be found around 3 TeV. Unfortunately, the Λ_9 scale, as well as all other high D scales, are not very sensitive to the $0\nu\beta\beta$ half-life, because they scale as $T_{1/2}^{\frac{1}{2(D-4)}}$. $\mathcal{O}_7$ and $\mathcal{O}_{11}$ provide small low-limits for Λ_7 and Λ_{11}. This feature is likely related to the fact that these terms are originating from small terms in the mixing matrix (e.g. the small S matrix in Eq. (A3) of [15]), and thus $g \sim 1$ in Eq. (18) is not a good choice. The most sensitive scale to both the unknown Yukawa and the $0\nu\beta\beta$ half-life is Λ_5. Assuming a Yukawa coupling corresponding to the electron mass, one can conclude that the $0\nu\beta\beta$ decay could be consistent with a new physics scale somewhere between 2 TeV and 20 TeV.

VII. CONCLUSIONS

This work advances and extends the analysis of BSM physics parameters involved in the neutrinoless double-beta decay. We calculate 20 nuclear matrix elements and 9 phase-space factors. Two of these nuclear matrix elements ($M_{GT'}$, $M_{T'}$) are calculated for the first time using shell model techniques. Three new hadron-level diagrams, Fig. 2.e, 2.f, 2.g are for the first time considered in the full analyses based on the effective field theory approach to $0\nu\beta\beta$ decay (they were only considered in the past in the context of particular mechanisms).

Using a general effective field theory and assuming that one LNV coupling plays a dominant contribution to the $0\nu\beta\beta$ decay amplitude, we extract limits for the effective Majorana mass and 11 effective low-energy couplings in the case of five nuclei of immediate experimental interest. Due to the better half-life limits, the most stringent limits for the LNV couplings are found for ^{136}Xe, closely followed by ^{76}Ge. An upper-limit for the Majorana neutrino mass $\langle m_{\beta\beta}\rangle$ of 140 meV was calculated in the case of ^{136}Xe. Assuming a Yukawa coupling corresponding to the electron mass, one can conclude that the $0\nu\beta\beta$ decay could be consistent with a new physics scale somewhere between 2 TeV and 20 TeV.

Using the upper limits for the LNV coupling we extract limits for the energy scale of the new physics, using EFT arguments. We found that the scale associated with the dimension-9 EFT operator is stable, and indicates a new physics scale around 3 TeV. We also found that the dimension-5 EFT operator associated with the Majorana neutrino mass varies significantly with the Yukawa coupling to Higgs and the $0\nu\beta\beta$ decay half-life.

If the neutrinoless double-beta decay process is experimentally confirmed, an analysis of possible contributions

TABLE XIII. Same as Table XII, for the short-range contribution to the $0\nu\beta\beta$ diagram, corresponding to the dimension 9 Lagrangian for the St-Ma set of Hamiltonians.

SRC	η_{LNV}	$\lvert\varepsilon_1\rvert \times 10^8$	$\lvert\varepsilon_2\rvert \times 10^{10}$	$\lvert\varepsilon_3^{RRz(LLz)}\rvert \times 10^9$	$\lvert\varepsilon_3^{LRz(RLz)}\rvert \times 10^9$	$\lvert\varepsilon_4\rvert \times 10^9$	$\lvert\varepsilon_5\rvert \times 10^8$	$\lvert\eta_{\pi N}\rvert \times 10^9$
CD-Bonn		6.77	4.12	3.12	5.19	3.62	3.28	1.61
AV-18		8.15	5.89	4.29	7.90	5.17	3.95	1.52
	$\mathcal{M}^2_{LNV}$	$\mathcal{M}^2_1 \times 10^{13}$	$\mathcal{M}^2_2 \times 10^8$	$\mathcal{M}^2_{3/LLz(RRz)} \times 10^{10}$	$\mathcal{M}^2_{3/LRz(RLz)} \times 10^{11}$	$\mathcal{M}^2_4 \times 10^{10}$	$\mathcal{M}^2_5 \times 10^{12}$	$\mathcal{M}^2_{\pi N} \times 10^{10}$
CD-Bonn	^{48}Ca	3.31	0.89	1.56	5.61	1.19	1.45	7.43
	^{76}Ge	1.47	0.40	0.70	2.55	0.57	0.68	3.01
	^{82}Se	5.38	1.46	2.56	9.26	1.96	2.36	11.3
	^{130}Te	12.0	3.25	5.68	20.5	4.22	5.11	21.3
	^{136}Xe	7.83	2.11	3.70	13.3	2.74	3.33	13.9
AV-18	^{48}Ca	2.28	0.43	0.82	2.40	0.58	1.00	8.21
	^{76}Ge	1.02	0.20	0.37	1.11	0.28	0.47	3.33
	^{82}Se	3.73	0.73	1.36	4.05	0.97	1.64	12.5
	^{130}Te	8.26	1.59	2.99	8.86	2.07	3.52	23.8
	^{136}Xe	5.41	1.04	1.95	5.75	1.34	2.30	15.5
	$T_{LNV} \times 10^{-26}$	T_1	T_2	$T_{3/RRz(LLz)}$	$T_{3/LRz(RLz)}$	T_4	T_5	$T_{\pi N}$
CD-Bonn	^{48}Ca	2.53	2.54	2.54	2.54	2.46	2.45	2.01
	^{76}Ge	5.68	5.61	5.62	5.58	5.18	5.25	4.96
	^{82}Se	1.56	1.54	1.55	1.54	1.50	1.51	1.32
	^{130}Te	0.70	0.70	0.70	0.69	0.69	0.70	0.70
AV-18	^{48}Ca	2.54	2.56	2.56	2.57	2.48	2.46	2.03
	^{76}Ge	5.67	5.57	5.59	5.52	5.14	5.24	4.99
	^{82}Se	1.55	1.53	1.53	1.52	1.48	1.50	1.33
	^{130}Te	0.70	0.70	0.70	0.69	0.69	0.70	0.70

TABLE XIV. The BSM effective scale (in GeV) for different dimension-D operators at the present ^{136}Xe half-life limit (Λ^0_D) and for $T_{1/2} \approx 1.1 \times 10^{28}$ years (Λ_D).

$\mathcal{O}_D$	$\bar{\epsilon}_D$	$\Lambda^0_D(y=1)$	$\Lambda^0_D(y=y_e)$	$\Lambda_D(y=y_e)$
$\mathcal{O}_5$	2.8×10^{-7}	2.12×10^{14}	1904	19044
$\mathcal{O}_7$	2.0×10^{-7}	3.76×10^4	542	1169
$\mathcal{O}_9$	9.3×10^{-8}	2.72×10^3	2718	4307
$\mathcal{O}_{11}$	9.3×10^{-8}	1.24×10^3	33	46

to the decay may be possible, based on the measured half-lives for different isotopes alone. The ratio of half-lives has been proposed before as a possible method for disentangling the heavy right-handed neutrino contribution from that of the light left-handed one. For this purpose, we performed an in-depth analysis of the ratio of half-lives for all 5 isotopes that are actively considered by experimentalists. We took into account the 12 contributions to the $0\nu\beta\beta$ described by the left-right symmetric model, the R-parity violating SUSY model, and an effective field theory. The study is presented under the assumption that only one contribution dominates. One main conclusion is that the nuclear matrix elements need to be calculated with better accuracy for most of the ratios to be relevant.

For a long time there were many debates in the literature regarding the uncertainties in the NME that originate from the treatment of the short-range correlations (SRC). Several methods and parametrization were developed for their inclusion in $0\nu\beta\beta$ calculations. Depending on the choice of the SRC method and parameters, the changes to the NME ranged from about 20% for the light left-handed neutrino exchange, to a dramatic 50% change in the case of the heavy right-handed neutrino exchange. In our investigation we found out that the SRC choice usually affects the half-life ratio only by around 1%, with the exception of the "$S+P/S\pm P$" and "TR/TR" cases. Based on this observation, we conclude that the SRC do not significantly affect our analysis of the half-life ratios calculated with ISM NME, as long as the choice is consistent for all isotopes considered. This conclusion does not diminish the importance and the need for obtaining an effective transition operator that properly takes into account the SRC effects in a consistent manner, rather just rules-out most of the uncertainty related to SRC for this particular type of analysis.

What was shown to have a great impact on our study was the choice of effective shell model Hamiltonians. It not only changes the extracted LNV couplings, but also places a large uncertainty over several half-life ratios. The isotopes considered here are calculated in three dif-

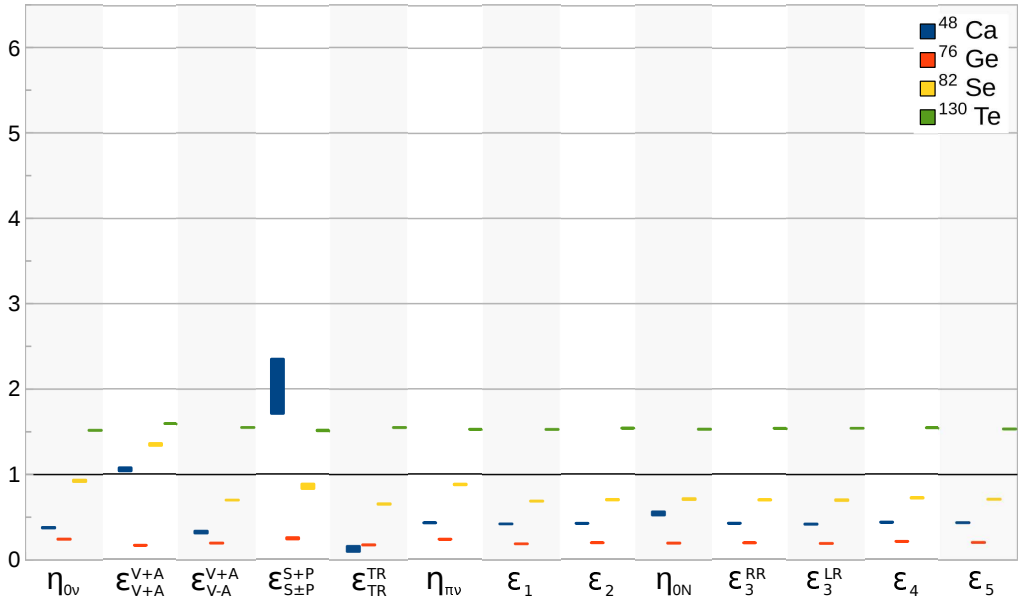

FIG. 4. Same as Fig. 3, but for the Strasbourg-Madrid choice of Hamiltonians.

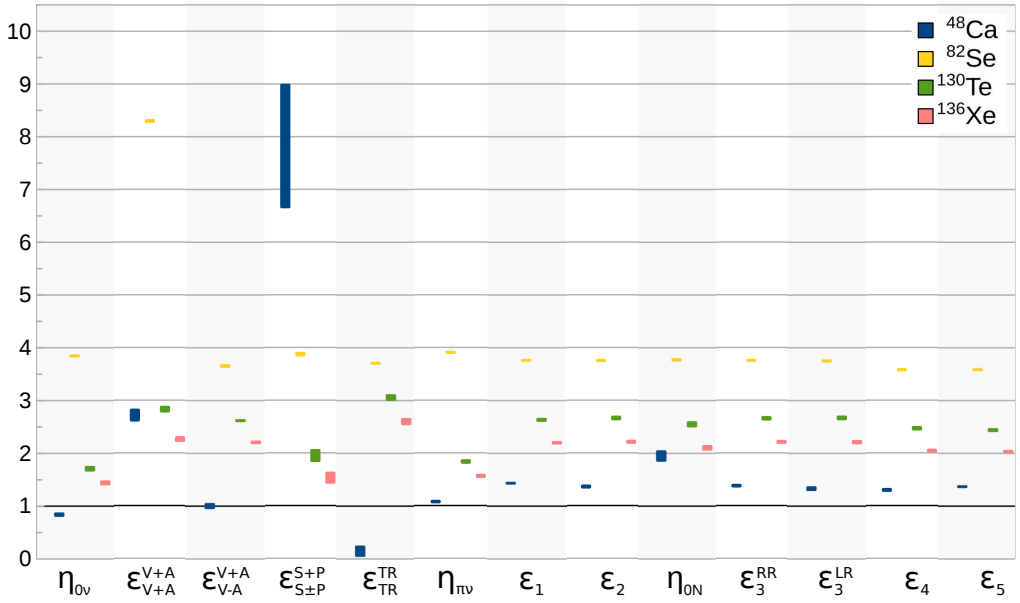

FIG. 5. Same as Fig. 3, but for ^{76}Ge instead of ^{136}Xe, with the CMU choice of Hamiltonians.

ferent model spaces, using a total of six effective Hamiltonians. It is not always possible to have half-life ratios for isotopes calculated in the same model space and using the same Hamiltonian. In the two cases where this is possible, the pairs ^{76}Ge–^{82}Se and ^{130}Te–^{136}Xe, the ratios spread and the consistency of the calculations is quite high. Unfortunately, the ratio between ^{130}Te and ^{136}Xe does not bring any information to this analysis, as it is constant, thus overlapping for all couplings. However, when choosing isotopes from different model spaces, the half-life ratios for a pair of isotopes can spread significantly. One extreme case is that of ^{136}Xe/^{82}Se for the ϵ^{V+A}_{V+A} contribution where the ratio spreads from 1.3, when using GCN 28:50 for ^{82}Se and GCN 50:82 for ^{136}Xe, to 3.6 in the case of JUN45 for ^{82}Se and SVD for ^{136}Xe.

Nevertheless, with our present analysis one could, in principle, distinguish several of the contributions to the $0\nu\beta\beta$ process that stand out beyond the uncertainties that arise from using the shell model Hamiltonians discussed. Ideally, more information could be extracted if the experimental half-lives of ^{48}Ca, ^{76}Ge, and ^{82}Se become available. The half-life ratio ^{76}Ge/^{48}Ca could indicate or rule-out the ϵ^{TR}_{TR} contribution and the $\epsilon^{S+P}_{S\pm P}$ con-

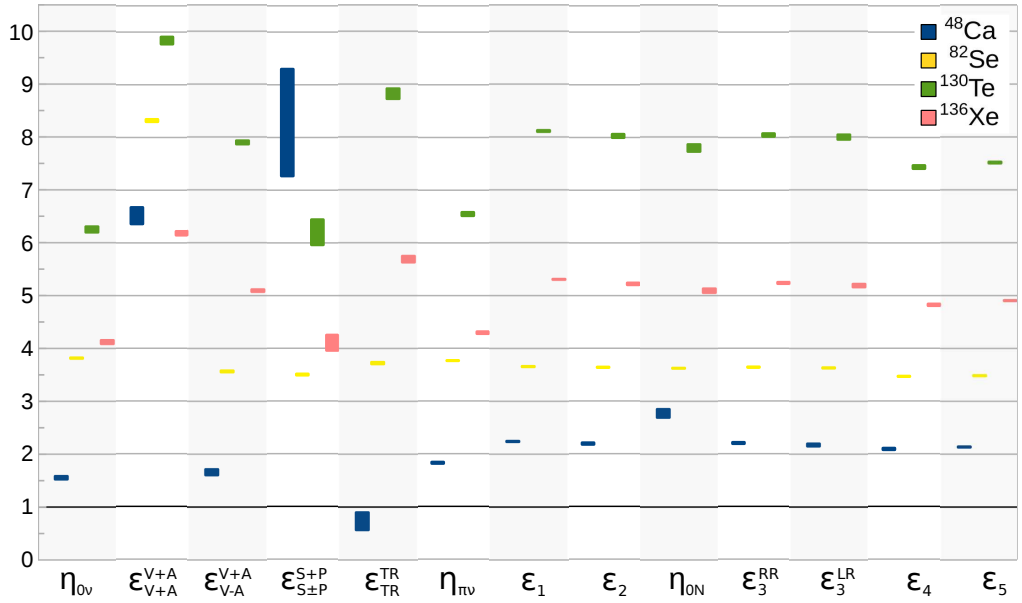

FIG. 6. Same as Fig. 5, but for the Strasbourg-Madrid effective Hamiltonians.

tribution. Another possible contribution, that of ϵ^{V+A}_{V+A} (also corresponding to the $\eta_\lambda-$mechanism), could be investigated by the ratio of ^{76}Ge/^{82}Se. If the tracking of the outgoing electrons will also become available, this complementary information could help decide the role of ϵ^{V+A}_{V-A} (also corresponding to the $\eta_\eta-$mechanism) [15].

Based on the figures presented, we conclude that once better and more consistent NME calculations become available, and with the complementary information from electron angular and energy distributions, it could be possible to distinguish all the couplings in the dimension-6 Lagrangian if the half-lives of several isotopes are measured. The half-life ratio corresponding to the couplings in the dimension-9 Lagrangian would still remain inseparable from the ratio corresponding to heavy right-handed neutrino exchange (ϵ^{RR}_3 in the EFT). Those need to be investigated via other methods, such as same charge dilepton production at LHC, etc.

VIII. APPENDIX

In this Appendix, we present the detailed expressions for the $\mathcal{M}^2_i$ coefficients that are needed to analyze the outcome of Eq. (5).

The NME that enter the equations (8, 10, 12, 14, and 16) are written as a product of two-body transition densities (TBTD) and two-body matrix elements (TBME), where the summation is over all the nucleon states. Their numerical values when calculated within the shell model approach are presented in Table XV for the light left-handed Majorana neutrino exchange, in Table XVI for the long-range part in Fig. 2, and in Table XVII for the short-range component of

TABLE XV. NME values for the exchange of light left-handed Majorana neutrinos corresponding to the diagram in Fig. 2b.

	^{48}Ca	^{76}Ge	^{82}Se	^{130}Te	^{136}Xe
M_{GT}	0.805	3.200	3.000	1.658	1.501
M_F	−0.233	−0.674	−0.632	−0.438	−0.400
M_T	0.073	0.011	0.012	−0.006	−0.007

Fig. 2. The general expressions for the NME are (see Refs. [15, 31, 62]):

$$M_\alpha = \sum_{j_p j_{p'} j_n j_{n'} J^\pi} TBTD\left(j_p j_{p'}, j_n j_{n'}; J^\pi\right) \times \left\langle j_p j_{p'}; J^\pi \left\| \tau_{-1}\tau_{-2}\mathcal{O}^{\gamma,\phi,\theta,P,R}_{12} \right\| j_n j_{n'}; J^\pi \right\rangle . \quad (20)$$

We group the operators that share similar structure into five families.

Gamow-Teller operator : $\mathcal{O}^{\gamma}_{12} = \vec{\sigma}_1 \cdot \vec{\sigma}_2 H_\gamma(r)$,

Fermi operator : $\mathcal{O}^{\phi}_{12} = H_\phi(r)$,

Tensor operator : $\mathcal{O}^{\theta}_{12} = [3(\vec{\sigma}_1 \cdot \hat{\mathbf{r}})(\vec{\sigma}_2 \cdot \hat{\mathbf{r}}) - \vec{\sigma}_1 \cdot \vec{\sigma}_2]\, H_\theta(r)$,

P operator : $\mathcal{O}^{P}_{12} = (\vec{\sigma}_1 - \vec{\sigma}_2)\, H_P(r)$,

R operator : $\mathcal{O}^{R}_{12} = \vec{\sigma}_1 \cdot \vec{\sigma}_2 H_R(r)$.

Here, $\gamma = GT,\ GT\omega,\ GTq,\ GTN,\ GT',\ GT\pi\nu,\ GT1\pi,\ GT2\pi,\ \phi = F,\ F\omega,\ Fq,\ FN$, and $\theta = T,\ Tq,\ T',\ T\pi\nu,\ T1\pi,\ T2\pi$. Equations (21) present the radial part of the NME and their expressions are adapted for consistency from Refs. [62],[23], and [82].

$$H_{GT} = \frac{2R}{\pi} \int \frac{h^2_{GT}(q^2)}{q(q+\bar{E})} j_0(qr) q^2 \, \mathrm{d}q \,, \quad (21a)$$

TABLE XVI. NME for the long-range part shown in Figs. 2c and 2e.

	^{48}Ca	^{76}Ge	^{82}Se	^{130}Te	^{136}Xe
M_{GTq}	0.709	3.228	3.034	1.587	1.440
$M_{GT\omega}$	0.930	3.501	3.287	1.855	1.682
$M_{GT'}$	0.841	2.699	2.567	2.120	1.935
$M_{GT\pi\nu}$	86.2	331.6	313.3	184.2	167.7
M_{Fq}	−0.121	−0.383	−0.362	−0.249	−0.230
$M_{F\omega}$	−0.232	−0.659	−0.618	−0.427	−0.391
M_{Tq}	−0.173	−0.059	−0.058	−0.013	−0.012
$M_{T'}$	0.337	0.015	0.025	−0.077	−0.085
$M_{T\pi\nu}$	21.29	7.28	6.89	1.22	1.12
M_P	0.390	−2.435	−2.303	−1.707	−1.597
M_R	1.001	3.243	3.088	2.530	2.312

TABLE XVII. The short-range NME involved in Figs. 2d, 2f, and 2g.

	^{48}Ca	^{76}Ge	^{82}Se	^{130}Te	^{136}Xe
M_{GTN}	55.9	156.5	144.9	103.0	92.6
$M_{GT1\pi}$	−1.354	−3.559	−3.282	−2.421	−2.171
$M_{GT2\pi}$	−0.676	−1.983	−1.854	−1.257	−1.137
M_{FN}	−22.9	−62.6	−58.1	−41.0	−36.9
$M_{T1\pi}$	−0.590	−0.010	−0.027	0.106	0.115
$M_{T2\pi}$	−0.227	−0.011	−0.015	0.038	0.041

$$H_{GT\omega} = \frac{2R}{\pi}\int \frac{h_A^2(q^2)}{(q+\bar{E})^2} j_0(qr) q^2 \,\mathrm{d}q\,, \tag{21b}$$

$$H_{GTq} = \frac{2R}{\pi} r \int \frac{h_A^2(q^2)}{q+\bar{E}} j_1(qr) q^2 \,\mathrm{d}q\,, \tag{21c}$$

$$H_{GTN} = \frac{2R}{\pi m_e m_p}\int h_A^2(q^2) j_0(qr) q^2 \,\mathrm{d}q\,, \tag{21d}$$

$$H_{GT'} = \frac{2R^2}{\pi m_p}\int \frac{q^2 h_A^2(q^2)}{q(q+\bar{E})} j_0(qr) q^2 \,\mathrm{d}q\,, \tag{21e}$$

$$H_{GT\pi\nu} = \frac{2R}{\pi}\int \frac{h_{GT\pi\nu}^2(q^2)}{q(q+\bar{E})} j_0(qr) q^2 \,\mathrm{d}q\,, \tag{21f}$$

$$H_{GT1\pi} = -\frac{2R}{\pi}\int h_A^2(q^2) \frac{q^2/m_\pi^4}{1+q^2/m_\pi^2} j_0(qr) q^2 \,\mathrm{d}q\,, \tag{21g}$$

$$H_{GT2\pi} = -\frac{4R}{\pi}\int h_A^2(q^2) \frac{q^2/m_\pi^4}{(1+q^2/m_\pi^2)^2} j_0(qr) q^2 \,\mathrm{d}q\,, \tag{21h}$$

$$H_F = \frac{2R}{\pi}\int \frac{h_V^2(q^2)}{q(q+\bar{E})} j_0(qr) q^2 \,\mathrm{d}q\,, \tag{21i}$$

$$H_{F\omega} = \frac{2R}{\pi}\int \frac{h_V^2(q^2)}{(q+\bar{E})^2} j_0(qr) q^2 \,\mathrm{d}q\,, \tag{21j}$$

$$H_{Fq} = \frac{2R}{\pi} r \int \frac{h_V^2(q^2)}{q+\bar{E}} j_1(qr) q^2 \,\mathrm{d}q\,, \tag{21k}$$

$$H_{FN} = \frac{2R}{\pi m_e m_p}\int h_V^2(q^2) j_0(qr) q^2 \,\mathrm{d}q\,, \tag{21l}$$

$$H_T = -\frac{2R}{\pi}\int \frac{h_T^2(q^2)}{q(q+\bar{E})} j_2(qr) q^2 \,\mathrm{d}q\,, \tag{21m}$$

$$H_{Tq} = \frac{2R}{3\pi}\sqrt{\frac{2}{3}} r C^{(2)}(\hat{\mathbf{r}}) \int \frac{h_A^2(q^2)}{q+\bar{E}} j_1(qr) q^2 \,\mathrm{d}q\,, \tag{21n}$$

$$H_{T'} = -\frac{2R^2}{\pi m_p}\int \frac{q^2 h_A^2(q^2)}{q(q+\bar{E})} j_2(qr) q^2 \,\mathrm{d}q\,, \tag{21o}$$

$$H_{T\pi\nu} = -\frac{2R}{\pi}\int \frac{h_{T\pi\nu}^2(q^2)}{q(q+\bar{E})} j_2(qr) q^2 \,\mathrm{d}q\,, \tag{21p}$$

$$H_{T1\pi} = \frac{2R}{\pi}\int h_A^2(q^2) \frac{q^2/m_\pi^4}{1+q^2/m_\pi^2} j_2(qr) q^2 \,\mathrm{d}q\,, \tag{21q}$$

$$H_{T2\pi} = \frac{4R}{\pi}\int h_A^2(q^2) \frac{q^2/m_\pi^4}{(1+q^2/m_\pi^2)^2} j_2(qr) q^2 \,\mathrm{d}q\,, \tag{21r}$$

$$H_R = \frac{(\mu_p-\mu_n)}{3}\frac{g_V}{g_A}\frac{2R^2}{\pi m_p} \times \int q \frac{h_A(q^2) h_V(q^2)}{q+\bar{E}} j_0(qr) q^2 \,\mathrm{d}q\,, \tag{21s}$$

$$H_P = \sqrt{2}\frac{2R}{\pi}\frac{g_V}{g_A} C^{(1)}(\hat{\mathbf{r}}) C^{(1)}(\hat{\mathbf{r}}_+) r_+ \times \int \frac{h_A(q^2) h_V(q^2)}{q+\bar{E}} j_1(qr) q^2 \,\mathrm{d}q\,,. \tag{21t}$$

Here, the expressions of $C_M^{(L)}$ and $\mathbf{r}$ of Eqs. (21n, 21t) are:

$$C_M^{(L)} = \sqrt{\frac{4\pi}{2L+1}} Y_{LM},$$

$$\mathbf{r} = \mathbf{r_1} - \mathbf{r_2}, \qquad \mathbf{r}_+ = \frac{\mathbf{r_1}+\mathbf{r_2}}{2}, \qquad r = |\mathbf{r}|,$$
$$\hat{\mathbf{r}} = \frac{\mathbf{r}}{r}, \qquad r_+ = |\mathbf{r}_+|, \qquad \hat{\mathbf{r}}_+ = \frac{\mathbf{r}_+}{r_+}.$$

The finite-size effects are taken into account via the following dipole form-factors:

$$g_A(q^2) = \left(\frac{\lambda_A^2}{\lambda_A^2+q^2}\right)^2, \tag{22a}$$

$$g_V(q^2) = \left(\frac{\lambda_V^2}{\lambda_V^2+q^2}\right)^2, \tag{22b}$$

$$g_M(q^2) = (\mu_p-\mu_n)\, g_V(q^2). \tag{22c}$$

Here $\lambda_A = 1086$ MeV and $\lambda_V = 850$ MeV are the axial and vector momentum cutoffs, respectively, and $(\mu_p - \mu_n) \simeq 3.7$.

The form-factors entering Eqs. 21 are:

$$h_V(q^2) = g_V(q^2), \tag{23a}$$

$$h_A(q^2) = g_A(q^2), \tag{23b}$$

$$h_{GT}^2(q^2) = g_A^2(q^2)\left[1 - \frac{2}{3}\frac{q^2}{q^2+{m_\pi}^2} + \frac{1}{3}\left(\frac{q^2}{q^2+m_\pi^2}\right)^2\right] + \frac{2}{3}\frac{g_M^2(q^2)}{g_A^2}\frac{q^2}{4m_p^2}, \tag{23c}$$

$$h_T^2(q^2) = g_A^2(q^2)\left[\frac{2}{3}\frac{q^2}{q^2+{m_\pi}^2} - \frac{1}{3}\left(\frac{q^2}{q^2+m_\pi^2}\right)^2\right] + \frac{1}{3}\frac{g_M^2(q^2)}{g_A^2}\frac{q^2}{4m_p^2}, \quad (23d)$$

$$h_{GT\pi\nu}^2(q^2) = -\frac{g_A^2(q^2)}{6}\frac{m_\pi^4}{m_e(m_u+m_d)}\frac{q^2}{(q^2+m_\pi^2)^2}, \quad (23e)$$

$$h_{T\pi\nu}^2(q^2) = h_{GT\pi\nu}^2(q^2). \quad (23f)$$

$m_e = 0.511$ MeV is the electron mass, $m_\pi = 139$ MeV is the pion mass, $m_p = 938$ MeV is the proton mass, and the quark masses sum is $(m_u + m_d) = 11.6$ MeV [31, 96].

The NME presented in this section (Eq. (20)) are calculated using shell model approaches. To take into account the two-nucleon short-range correlation (SRC) we multiply the relative wave functions by $f(r) = 1 - ce^{-ar^2}(1 - br^2)$; in the CD-Bonn parametrization used here $a = 1.52$ fm^{-2}, $b = 1.88$ fm^{-2}, and $c = 0.46$ fm^{-2} [97]. This method is described in greater detail in Refs. [31, 36–41, 43–46]. The signs of all the NME presented in the following tables are relative to the sign of M_{GT}, which is taken to be positive. Table XV presents the M_{GT}, M_F, and M_T NME involved in the standard mass mechanism with left-handed currents of Eq. (8). For these NME, an optimal closure energy $\langle \bar{E} \rangle$ was used for each effective Hamiltonian [40]: $\langle \bar{E} \rangle = 0.5$ MeV for ^{48}Ca [38] and the GXPF1A Hamiltonian [98], $\langle \bar{E} \rangle = 3.4$ MeV for ^{76}Ge [60] and ^{82}Se [40] calculated with the JUN45 Hamiltonian [64], and $\langle \bar{E} \rangle = 3.5$ MeV for ^{130}Te [44] and ^{136}Xe [39] calculated with the SVD Hamiltonian [65].

The long-range NME M_α (with $\alpha = GTq$, Fq, Tq, $GT\omega$, $F\omega$, P, R, GT', T') that appear in Eq. (10) and $M_{GT\pi\nu}$ and $M_{T\pi\nu}$ of Eq. (12) are presented in Table XVI.

Shown in Table XVII are the short-range NME M_{GTN} and M_{FN} that appear in Eq. (14 and M_α (with $\alpha = GT1\pi$, $T1\pi$, $GT2\pi$, $T2\pi$) in Eq. 16).

IX. ACKNOWLEDGMENTS

Support from the NUCLEI SciDAC Collaboration under U.S. Department of Energy Grant No. DE-SC0008529 and DE-SC0008641 is acknowledged. M. Horoi also acknowledges the U.S. NSF Grant No. PHY-1404442 and the U.S. Department of Energy Grant No. DE-SC0015376.

[1] Y. Fukuda, T. Hayakawa, E. Ichihara, K. Inoue, K. Ishihara, H. Ishino, Y. Itow, T. Kajita, J. Kameda, S. Kasuga, et al. (Super-Kamiokande Collaboration), Phys. Rev. Lett. **81**, 1562 (1998), URL https://link.aps.org/doi/10.1103/PhysRevLett.81.1562.

[2] Q. R. Ahmad, R. C. Allen, T. C. Andersen, J. D. Anglin, G. Bühler, J. C. Barton, E. W. Beier, M. Bercovitch, J. Bigu, S. Biller, et al. (SNO Collaboration), Phys. Rev. Lett. **87**, 071301 (2001), URL https://link.aps.org/doi/10.1103/PhysRevLett.87.071301.

[3] T. Kajita, *Discovery of atmospheric neutrino oscillations*, http://www.nobelprize.org/nobel_prizes/physics/laureates/2015/kajita-lecture.pdf (2015).

[4] Arthur B. McDonald, *The Sudbury Neutrino Observatory: Observation of Flavor Change for Solar Neutrinos*, http://www.nobelprize.org/nobel_prizes/physics/laureates/2015/mcdonald-lecture.pdf (2015).

[5] J. Schechter and J. W. F. Valle, Phys. Rev. D **25**, 2951 (1982).

[6] J. Nieves, Phys. Lett. B **147**, 375 (1984).

[7] E. Takasugi, Phys. Lett. B **149**, 372 (1984).

[8] M. Hirsch, S. Kovalenko, and I. Schmidt, Phys. Lett. B **642**, 106 (2006).

[9] J. Pati and A. Salam, Phys. Rev. D **10**, 275 (1974).

[10] R. Mohapatra and J. Pati, Phys. Rev. D **11**, 2558 (1975).

[11] G. Senjanovic and R. N. Mohapatra, Phys. Rev. D **12**, 1502 (1975).

[12] W.-Y. Keung and G. Senjanovic, Phys. Rev. Lett. **50**, 1427 (1983).

[13] J. Barry and W. Rodejohann, J. High Energy Phys. p. 153 (2013).

[14] V. Khachatryan, A. M. Sirunyan, A. Tumasyan, W. Adam, T. Bergauer, M. Dragicevic, J. Er, C. Fabjan, M. Friedl, R. Fruhwirth, et al. (CMS-Collaboration), Eur. Phys. J. C **74**, 3149 (2014).

[15] M. Horoi and A. Neacsu, Phys. Rev. D **93**, 113014 (2016), arXiv:1511.00670 [hep-ph].

[16] A. Neacsu and M. Horoi, Advances in High Energy Physics **2016** (2016).

[17] V. Cirigliano, W. Dekens, J. de Vries, M. L. Graesser, and E. Mereghetti (2017), arXiv:1708.09390.

[18] V. Cirigliano, W. Dekens, M. Graesser, and E. Mereghetti, Physics Letters B **769**, 460 (2017), ISSN 0370-2693, URL http://www.sciencedirect.com/science/article/pii/S0370269317302940.

[19] E. Berkowitz, D. Brantley, C. Bouchard, C. C. Chang, M. A. Clark, N. Garron, B. Joo, T. Kurth, C. Monahan, H. Monge-Camacho, et al. (2017), arXiv:1704.01114.

[20] M. Hirsch, H. V. Klapdor-Kleingrothaus, and S. G. Kovalenko, Phys. Lett. B **372**, 181 (1996), hep-ph/9512237.

[21] H. Pas, M. Hirsch, H. V. Klapdor-Kleingrothaus, and S. G. Kovalenko, Phys. Lett. B **453**, 194 (1999).

[22] H. Pas, M. Hirsch, H. V. Klapdor-Kleingrothaus, and S. G. Kovalenko, Phys. Lett. B **498**, 35 (2001), hep-ph/0008182.

[23] F. F. Deppisch, M. Hirsch, and H. Pas, J. Phys. G **39**, 124007 (2012).

[24] F. Simkovic, G. Pantis, J. D. Vergados, and A. Faessler, Phys. Rev. C **60**, 055502 (1999).

[25] J. Suhonen and O. Civitarese, Nucl. Phys. A **847**, 207 (2010).

[26] A. Faessler, A. Meroni, S. T. Petcov, F. Simkovic, and J. Vergados, Phys. Rev. D **83**, 113003 (2011).

[27] M. T. Mustonen and J. Engel, Phys. Rev. C **87**, 064302 (2013).
[28] A. Faessler, M. Gonzalez, S. Kovalenko, and F. Simkovic, Phys. Rev. D **90**, 096010 (2014).
[29] J. Retamosa, E. Caurier, and F. Nowacki, Phys. Rev. C **51**, 371 (1995).
[30] E. Caurier, F. Nowacki, A. Poves, and J. Retamosa, Phys. Rev. Lett. **77**, 1954 (1996).
[31] M. Horoi, Phys. Rev. C **87**, 014320 (2013).
[32] A. Neacsu and S. Stoica, Advances in High Energy Physics **2014** (2014).
[33] E. Caurier, J. Menendez, F. Nowacki, and A. Poves, Phys. Rev. Lett. **100**, 052503 (2008).
[34] J. Menendez, A. Poves, E. Caurier, and F. Nowacki, Nucl. Phys. A **818**, 139 (2009).
[35] E. Caurier, G. Martinez-Pinedo, F. Nowacki, A. Poves, and A. P. Zuker, Rev. Mod. Phys. **77**, 427 (2005).
[36] M. Horoi and S. Stoica, Phys. Rev. C **81**, 024321 (2010).
[37] A. Neacsu, S. Stoica, and M. Horoi, Phys. Rev. C **86**, 067304 (2012).
[38] R. A. Sen'kov and M. Horoi, Phys. Rev. C **88**, 064312 (2013).
[39] M. Horoi and B. A. Brown, Phys. Rev. Lett. **110**, 222502 (2013).
[40] R. A. Sen'kov, M. Horoi, and B. A. Brown, Phys. Rev. C **89**, 054304 (2014).
[41] B. A. Brown, M. Horoi, and R. A. Sen'kov, Phys. Rev. Lett. **113**, 262501 (2014).
[42] A. Neacsu and S. Stoica, J. Phys. G **41**, 015201 (2014).
[43] R. A. Sen'kov and M. Horoi, Phys. Rev. C **90**, 051301(R) (2014).
[44] A. Neacsu and M. Horoi, Phys. Rev. C **91**, 024309 (2015).
[45] M. Horoi and A. Neacsu, Phys. Rev. C **93**, 024308 (2016).
[46] M. Horoi, S. Stoica, and B. A. Brown, Phys. Rev. C **75**, 034303 (2007).
[47] M. Blennow, E. Fernandez-Martinez, J. Lopez-Pavon, and J. Menendez, JHEP **07**, 096 (2010).
[48] J. Barea and F. Iachello, Phys. Rev. C **79**, 044301 (2009).
[49] J. Barea, J. Kotila, and F. Iachello, Phys. Rev. Lett. **109**, 042501 (2012).
[50] J. Barea, J. Kotila, and F. Iachello, Phys. Rev. C **87**, 014315 (2013).
[51] J. Barea, J. Kotila, and F. Iachello, Phys. Rev. C **91**, 034304 (2015).
[52] P. K. Rath, R. Chandra, K. Chaturvedi, P. Lohani, P. K. Raina, and J. G. Hirsch, Phys. Rev. C **88**, 064322 (2013).
[53] T. R. Rodriguez and G. Martinez-Pinedo, Phys. Rev. Lett. **105**, 252503 (2010).
[54] L. S. Song, J. M. Yao, P. Ring, and J. Meng, Phys. Rev. C **90**, 054309 (2014).
[55] A. Faessler, V. Rodin, and F. Simkovic, J. Phys. G **39**, 124006 (2012).
[56] P. Vogel, J. Phys. G **39**, 124002 (2012).
[57] F. Simkovic, V. Rodin, A. Faessler, and P. Vogel, Phys. Rev. C **87**, 045501 (2013).
[58] J. Hyvarinen and J. Suhonen, Phys. Rev. C **91**, 024613 (2015).
[59] J. D. Holt and J. Engel, Phys. Rev. C **87**, 064315 (2013).
[60] R. A. Sen'kov and M. Horoi, Phys. Rev. C **93**, 044334 (2016).
[61] B. A. Brown, D. L. Fang, and M. Horoi, Phys. Rev. C **92**, 041301 (2015).
[62] M. Doi, T. Kotani, and E. Takasugi, Prog. Theor. Phys. Suppl. **83**, 1 (1985).
[63] M. Honma, T. Otsuka, B. A. Brown, and T. Mizusaki, Phys. Rev. C **69**, 034335 (2004).
[64] M. Honma, T. Otsuka, T. Mizusaki, and M. Hjorth-Jensen, Phys. Rev. C **80**, 064323 (2009).
[65] C. Qi and Z. X. Xu, Phys. Rev. C **86**, 044323 (2012).
[66] A. Poves, J. Snchez-Solano, E. Caurier, and F. Nowacki, Nuclear Physics A **694**, 157 (2001), ISSN 0375-9474, URL `http://www.sciencedirect.com/science/article/pii/S0375947401009678`.
[67] S. Stoica and M. Mirea, Phys. Rev. C **88**, 037303 (2013).
[68] R. Arnold, C. Augier, A. M. Bakalyarov, J. D. Baker, A. S. Barabash, A. Basharina-Freshville, S. Blondel, S. Blot, M. Bongrand, V. Brudanin, et al. (NEMO-3 Collaboration), Phys. Rev. D **93**, 112008 (2016).
[69] M. Agostini et al. (GERDA), in *15th International Conference on Topics in Astroparticle and Underground Physics (TAUP 2017) Sudbury, Ontario, Canada, July 24-28, 2017* (2017), 1710.07776, URL `https://inspirehep.net/record/1632043/files/arXiv:1710.07776.pdf`.
[70] *Latest results from NEMO-3 and status of the SuperNEMO Experiment* (2016), `http://neutrino2016.iopconfs.org/IOP/media/uploaded/EVIOP/event_948/10.25__5__waters.pdf`.
[71] K. Alfonso, D. R. Artusa, F. T. Avignone, O. Azzolini, M. Balata, T. I. Banks, G. Bari, J. W. Beeman, F. Bellini, A. Bersani, et al. (CUORE Collaboration), Phys. Rev. Lett. **115**, 102502 (2015), URL `http://link.aps.org/doi/10.1103/PhysRevLett.115.102502`.
[72] A. Gando, Y. Gando, T. Hachiya, A. Hayashi, S. Hayashida, H. Ikeda, K. Inoue, K. Ishidoshiro, Y. Karino, M. Koga, et al. (KamLAND-Zen Collaboration), Phys. Rev. Lett. **117**, 082503 (2016), URL `https://link.aps.org/doi/10.1103/PhysRevLett.117.082503`.
[73] M. Doi, T. Kotani, H. Nishiura, and E. Takasugi, Progr. Theor. Exp. Phys. **69**, 602 (1983).
[74] W. Rodejohann, J. Phys. G **39**, 124008 (2012).
[75] R. N. Mohapatra and J. C. Pati, Phys. Rev. D **11**, 566 (1975).
[76] M. Hirsch, H. KlapdorKleingrothaus, and S. Kovalenko, Phys. Rev. D **53**, 1329 (1996).
[77] S. Kolb, M. Hirsch, and H. V. Klapdor-Kleingrothaus, Phys. Rev. D **56**, 4161 (1997).
[78] A. Faessler, T. Gutsche, S. Kovalenko, and F. Šimkovic, Phys. Rev. D **77**, 113012 (2008).
[79] J. Suhonen and O. Civitarese, Phys. Rep. **300**, 123 (1998).
[80] J. Kotila and F. Iachello, Phys. Rev. C **85**, 034316 (2012).
[81] M. Horoi and A. Neacsu, Adv. High Energy Phys. **2016**, 7486712 (2016).
[82] J. D. Vergados, H. Ejiri, and F. Simkovic, Rep. Prog. Phys. **75**, 106301 (2012).
[83] P. S. Bhupal Dev, S. Goswami, and M. Mitra, Phys. Rev. D **91**, 113004 (2015).
[84] D. Stefanik, R. Dvornicky, F. Simkovic, and P. Vogel, Phys. Rev. C **92**, 055502 (2015), arXiv:1506.07145 [hep-ph].
[85] K. Muto, E. Bender, and H. Klapdor, Z. Phys. A - Atomic Nuclei **334**, 187 (1989).
[86] A. Faessler and F. Simkovic, Journal of Physics G: Nuclear and Particle Physics **24**, 2139 (1998), URL `http://stacks.iop.org/0954-3899/24/i=12/a=001`.

[87] V. Cirigliano, *Private communication to M. Horoi* (2018).
[88] A. Wodecki, W. A. Kamiński, and F. Šimkovic, Phys. Rev. D **60**, 115007 (1999).
[89] G. Prezeau, M. Ramsey-Musolf, and P. Vogel, Phys.Rev. D **68**, 034016 (2003).
[90] T. Peng, M. J. Ramsey-Musolf, and P. Winslow, Phys. Rev. D **93**, 093002 (2016).
[91] F. F. Deppisch, J. Harz, W.-C. Huang, M. Hirsch, and H. Päs, Phys. Rev. D **92**, 036005 (2015).
[92] F. Ahmed, A. Neacsu, and M. Horoi, Physics Letters B **769**, 299 (2017).
[93] Z. Maki, M. Nakagawa, and S. Sakata, Prog. Theor. Phys. **28**, 870 (1962), URL `http://dx.doi.org/10.1143/PTP.28.870`.
[94] J. Beringer, J. F. Arguin, R. M. Barnett, K. Copic, O. Dahl, D. E. Groom, C. J. Lin, J. Lys, H. Murayama, C. G. Wohl, et al. (Particle Data Group), Phys. Rev. D **86**, 010001 (2012).
[95] S. L. Adler, E. W. Colglazier, J. B. Healy, I. Karliner, J. Lieberman, Y. J. Ng, and H. S. Tsao, Phys. Rev. D **11**, 3309 (1975), URL `http://link.aps.org/doi/10.1103/PhysRevD.11.3309`.
[96] A. Faessler, S. Kovalenko, and F. Šimkovic, Phys. Rev. D **58**, 115004 (1998).
[97] F. Simkovic, A. Faessler, H. Muether, V. Rodin, and M. Stauf, Phys. Rev. C **79**, 055501 (2009).
[98] M. Honma, T. Otsuka, B. A. Brown, and T. Mizusaki, Eur. Phys. J. A **25 Suppl. 1**, 499 (2005).